bioRxiv preprint doi: https://doi.org/10.1101/2020.09.18.301481; this version posted September 18, 2020. The copyright holder for this preprint (which was not certified by peer review) is the author/funder, who has granted bioRxiv a license to display the preprint in perpetuity. It is made available under aCC-BY-NC-ND 4.0 International license.

Cortical actin properties controlled by *Drosophila* Fos aid macrophage infiltration against surrounding tissue resistance

Short title: Macrophage Cortical Actin counteracts Tissue Resistance

Vera Belyaeva[§1,2], Stephanie Wachner[§1], Igor Gridchyn[†1], Markus Linder[†3,4], Shamsi Emtenani[1], Attila Gyoergy[1], Maria Sibilia[3], Daria Siekhaus[1*]

§: These authors contributed equally

†: These authors contributed equally

*- Corresponding author, *daria.siekhaus@ist.ac.at*

1 – Institute of Science and Technology Austria, Am Campus 1, 3400 Klosterneuburg, Austria

2 – Current address: Molecular Devices, Urstein Süd 17, 5412, Austria

3 – Institute of Cancer Research, Department of Medicine 1, Comprehensive Cancer Center, Medical University of Vienna, Austria

4 – Current address: F. Hoffmann - La Roche Ltd.,Grenzacherstrasse 124, 4070 Basel, Switzerland

bioRxiv preprint doi: https://doi.org/10.1101/2020.09.18.301481; this version posted September 18, 2020. The copyright holder for this preprint (which was not certified by peer review) is the author/funder, who has granted bioRxiv a license to display the preprint in perpetuity. It is made available under aCC-BY-NC-ND 4.0 International license.

ABSTRACT

The infiltration of immune cells into tissues underlies the establishment of tissue resident macrophages, and responses to infections and tumors. Yet the mechanisms immune cells utilize to negotiate tissue barriers in living organisms are not well understood, and a role for cortical actin has not been examined. Here we find that the tissue invasion of *Drosophila* macrophages, also known as plasmatocytes or hemocytes, utilizes enhanced cortical F-actin levels stimulated by the *Drosophila* member of the fos proto oncogene transcription factor family (Dfos, Kayak). RNA sequencing analysis and live imaging show that Dfos enhances F-actin levels around the entire macrophage surface by increasing mRNA levels of the membrane spanning molecular scaffold tetraspanin TM4SF, and the actin cross-linking filamin Cheerio which are themselves required for invasion. Cortical F-actin levels are critical as expressing a dominant active form of Diaphanous, a actin polymerizing Formin, can rescue the *Dfos* Dominant Negative macrophage invasion defect. *In vivo* imaging shows that Dfos is required to enhance the efficiency of the initial phases of macrophage tissue entry. Genetic evidence argues that this Dfos-induced program in macrophages counteracts the constraint produced by the tension of surrounding tissues and buffers the mechanical properties of the macrophage nucleus from affecting tissue entry. We thus identify tuning the cortical actin cytoskeleton through Dfos as a key process allowing efficient forward movement of an immune cell into surrounding tissues.

Introduction

The classical model of cell migration on a surface postulated in the 1980's by Abercrombie has been extended (Danuser et al., 2013) by studies showing that migrating cells utilize diverse strategies depending on the architecture and physical properties of their three dimensional (3D) surroundings (Paluch et al., 2016). Much of this work has been

bioRxiv preprint doi: https://doi.org/10.1101/2020.09.18.301481; this version posted September 18, 2020. The copyright holder for this preprint (which was not certified by peer review) is the author/funder, who has granted bioRxiv a license to display the preprint in perpetuity. It is made available under aCC-BY-NC-ND 4.0 International license.

conducted *in vitro*, where variations in the environment can be strictly controlled. However most 3D migration occurs within the body, and much less research has elucidated the mechanisms used to efficiently move in these diverse environments, particularly into and through tissues. Such migration is crucial for the influence of the immune system on health and disease. Vertebrate macrophages migrate into tissues during development where they take up residence, regulating organ formation and homeostasis and organizing tissue repair upon injury (Ginhoux and Guilliams, 2016; Theret et al 2019). A variety of types of immune cells infiltrate into tumors, and can both promote or impede cancer progression (Greten and Grivennikov 2019; Sharma and Allison, 2015). Responses to infection require immune cells to traverse through the vascular wall, into the lymph node, and through tissues (Luster et al., 2005). Yet the mechanisms utilized by immune cells to allow migration into such challenging cellular environments *in vivo* are not well understood.

Migration in 2-D and 3-D environments utilizes actin polymerization to power forward progress. The assembly of actin at the leading edge, when coupled to Integrin adhesion to anchor points in the surrounding ECM, can allow the front of the cell to progress (Mitchison and Cramer, 1996). This anchoring also allows the contraction of cortical actin at the rear plasma membrane to bring the body of the cell forwards. But a role for crosslinked actin at the cell surface in assisting forward progress by helping to counteract the resistance of surrounding tissues and in buffering nuclear properties has not been previously identified.

Our lab utilizes *Drosophila* macrophage migration into the embryonic germband (gb) to investigate mechanisms of immune cell tissue invasion. Macrophages, also called plasmatocytes or hemocytes, are the primary phagocytic cell in *Drosophila* and share striking similarities with vertebrate macrophages (Brückner et al., 2004; Evans & Wood, 2011; Lemaitre & Hoffmann, 2007; Ratheesh et al., 2015; Weavers et al., 2016). They are

bioRxiv preprint doi: https://doi.org/10.1101/2020.09.18.301481; this version posted September 18, 2020. The copyright holder for this preprint (which was not certified by peer review) is the author/funder, who has granted bioRxiv a license to display the preprint in perpetuity. It is made available under aCC-BY-NC-ND 4.0 International license.

specified in the head mesoderm at embryonic stages 4-6 and by stage 10 start spreading along predetermined routes guided by platelet-derived growth factor- and vascular endothelial growth factor-related factors (Pvf) 2 and 3 (Cho et al., 2002; Brückner et al., 2004; Wood et al., 2006) to populate the whole embryo. One of these paths, the movement into the gb, requires macrophages to invade confined between the ectoderm and mesoderm (Ratheesh et al., 2018; Siekhaus et al., 2010). The level of tension and thus apparent stiffness of the flanking ectoderm is a key parameter defining the efficiency of macrophage passage into and within the gb (Ratheesh et al., 2018). Penetration of macrophages into the gb utilizes Integrin, occurs normally without MMPs (Siekhaus et al., 2010) and is even enhanced by ECM deposition (Valoskova et al., 2019; Sánchez-Sánchez et al., 2017) likely because the basement membrane has not yet formed at this stage (Matsubayashi et al., 2017; Ratheesh et al., 2018). Thus *Drosophila* macrophage gb invasion represents an ideal system to explore the mechanisms by which immune cells and surrounding tissues interact with one another to aid the invasion process.

Here we sought to identify a transcription factor that could control immune cell tissue invasion and elucidate its downstream mechanisms. We identify a role for the *Drosophila* ortholog of the proto-oncogene Fos, in initial entry and migration within the tissue. We find Dfos increases cortical macrophage F-actin levels through the formin Cheerio and the novel target the tetraspanin TM4SF, aiding macrophages to move forward against the resistance of the surrounding tissues while buffering the mechanical properties of the nucleus.

Results

The transcription factor Dfos is required for macrophage germband invasion

To identify regulators of programs for invasion we searched the literature for transcription factors in macrophages prior to or during their invasion of germband tissues (gb) (Fig 1A-B'). Of the 12 such factors (S1 Table, based on Hammonds et al., 2013) we

bioRxiv preprint doi: https://doi.org/10.1101/2020.09.18.301481; this version posted September 18, 2020. The copyright holder for this preprint (which was not certified by peer review) is the author/funder, who has granted bioRxiv a license to display the preprint in perpetuity. It is made available under aCC-BY-NC-ND 4.0 International license.

focused on Dfos, a member of the Fos proto-oncogene family, assigned by the Roundup algorithm as being closest to vertebrate c-fos (Deluca et al., 2012; Thurmond et al., 2019) (Fig 1C). Dfos contains the basic leucine zipper domain (bZIP) shown to mediate DNA binding and hetero and homo dimerization (Glover and Harrison, 1995; Szalóki et al., 2015) with the third leucine replaced by a methionine, a position also altered in the *C. elegans* ortholog FOS-1A (Sherwood et al., 2005). Embryo *in situ* hybridizations reveal enriched expression of the gene in macrophages at early stage 11 (Fig 1D, arrow) which is attenuated by stage 13. Dfos protein appears in the nucleus in a subset of the macrophages that are migrating towards the gb at stage 10-11 and in all macrophages by early stage 12 (Fig 1E-F' yellow arrowheads, G-G"' white arrows) persisting through stage 13 (S1A Fig). The $Dfos^{1}$ null mutant eliminates the macrophage signal, indicating antibody specificity (Fig 1H). To determine if Dfos affects invasion, we examined the 70% of embryos from $Dfos^{1}$ and the hypomorph $Dfos^{2}$ that did not display developmental defects at these early stages; we quantified macrophage numbers in the gb during a defined development period in early stage 12 (Fig 1M). Both Dfos mutants displayed significantly reduced numbers of macrophages in the gb compared to the control (Fig 1I-K, N) with normal numbers in the pre-gb zone for $Dfos^{2}$ (S1B Fig) (S1 Data). Macrophage-specific expression of *Dfos* rescues the $Dfos^{2}$ mutant (Fig 1L,N). Blocking Dfos function in macrophages with a dominant negative (DN) Dfos (Fig 1O-Q) that lacks the activation domain but retains the capacity to dimerize and bind DNA (Eresh et al., 1997) or two different RNAis against *Dfos* (Fig 1R) recapitulates the decrease in gb macrophages seen in the null while not affecting macrophage numbers in the whole embryo (S1C Fig), neighboring the germband (S1D Fig) and along the ventral nerve cord (vnc); (S1E-F Fig). These results argue that Dfos is required in macrophages for their migration into the gb. Since overexpressing DfosDN in the midgut does not inhibit a bZIP protein that acts there (Eresh et al., 1997) and

bioRxiv preprint doi: https://doi.org/10.1101/2020.09.18.301481; this version posted September 18, 2020. The copyright holder for this preprint (which was not certified by peer review) is the author/funder, who has granted bioRxiv a license to display the preprint in perpetuity. It is made available under aCC-BY-NC-ND 4.0 International license.

overexpressing Dfos in macrophages does not change gb numbers (S1G Fig), Dfos and DfosDN do not appear to inhibit other bZIP proteins at higher levels of expression. As DfosDN should exert a quicker effect than RNAis, further experiments examining Dfos' role in enhancing germband invasion utilized mostly the DN form.

Fig 1. The bZIP transcription factor Dfos acts in macrophages to facilitate their migration into the germband

Schematics of lateral **(A)** stage (St) 11 and **(A')** early St 12 embryos. The boxed region magnified below indicates where macrophages (green) invade the germband (gb) after moving there from the head **(B-B')**. Macrophages sit on the yolk sac (yellow) next to the amnioserosa (black llne) and then invade between the ectoderm (blue) and mesoderm (purple).

(C) Dfos protein aligned with its human orthologs c-Fos and FosB; orange outlines the bZIP region that has 48% identity to both proteins: identical amino acids shown in orange, conserved ones in green. Stars indicate Leucines in the zipper; ^ the third leucine which in Dfos is a methionine, a tolerated substitution (Garcia-Echeverria, 1997). The lower solid line indicates the basic domain and the dotted line the leucine zipper (ZIP).

(D) *In situ* hybridization of St 11 and 13 embryos with a riboprobe for Dfos-RB (Fbcl0282531) which also detects all Dfos isoforms. *Dfos* RNA expression is enriched in macrophages (arrow) and the amnioserosa (arrowhead) before gb invasion, but is gone thereafter.

(E-H') Confocal images of the boxed region in A from fixed embryos expressing *GFP* in macrophages (green) stained with a Dfos Ab (red). **(E-F', H-H')** A white dashed line indicates the gb edge. **(E-F)** The Dfos Ab (yellow arrowheads) stains (**E**) a subset of the macrophages moving towards the gb at St 11, and **(F)** all macrophages by early St 12, as well as the amnioserosa (white arrowheads). **(G)** Higher magnification shows Dfos colocalizing with the nuclear marker DAPI (white). **(H)** No staining is detected in macrophages or the amnioserosa in the null $Dfos^{1}$ mutant.

(I-L) Lateral views of mid St 12 embryos from **(I)** the control, **(J)** the null allele $Dfos^{1}$, **(K)** the hypomorphic allele $Dfos^{2}$, and **(L)** $Dfos^{2}$ with *Dfos* re-expressed in macrophages.

bioRxiv preprint doi: https://doi.org/10.1101/2020.09.18.301481; this version posted September 18, 2020. The copyright holder for this preprint (which was not certified by peer review) is the author/funder, who has granted bioRxiv a license to display the preprint in perpetuity. It is made available under aCC-BY-NC-ND 4.0 International license.

(M) Schematic of St 12 embryo, gb region indicated by a black oval outline. **(N)** Quantitation reveals that both *Dfos* alleles display fewer macrophages in the gb. Re-expression of *Dfos* in macrophages in the $Dfos^2$ hypomorph significantly rescues the defect. Control vs. $Dfos^1$ p=0.02 (30% reduction), Control vs. $Dfos^2$ p=0.017 (25% reduction), Control vs. $Dfos^2$*; mac>Dfos* p=0.334.

(O-P) Lateral views of mid St 12 embryos from **(O)** the control, or **(P)** a line expressing a dominant negative (DN) form of Dfos in macrophages. **(Q)** Quantification of macrophage numbers in the gb (see schematic) in the two genotypes visualized in **O**, **P**. p<0.0001(****) (41% reduction).

(R) Quantification of macrophage numbers in the gb of the control and two different lines expressing RNAi constructs against Dfos in macrophages. Control vs. *Dfos* $RNAi^1$ (TRiP HMS00254) p=0.001 (32% reduction), Control vs. *Dfos* $RNAi^2$ (TRiP JF02804) p=0.02 (21% reduction). The data in **Q** and **R** argue that Dfos is required within macrophages to promote gb tissue invasion.

Embryos are positioned with anterior to left and dorsal up in all images and histograms show mean + standard error of the mean (SEM) throughout. Macrophages are labeled using *srp-Gal4* ("mac>") driving *UAS-GFP* in **E-H**, *UAS-GFP::nls* in **I-L** and *srpHemo-H2A::3xmCherry* in **O-P**. ***p<0.005, **p<0.01, *p<0.05. One-way ANOVA with Tukey post hoc was used for **N** and **R**, and unpaired t-test for **Q**. The embryo number analysed is indicated within the relevant column in the graphs. Scale bar: 50 μm in **D**, 5 μm in **E-H** and 10 μm in **I-L, O-P**.

Dfos promotes macrophage motility and persistence during tissue entry

To examine the dynamic effects of Dfos on tissue invasion, we performed live imaging and tracking of macrophages. We visualized macrophages with *srpHemo-H2A::3xmCherry* (Gyoergy et al., 2018) in either a wild type or *mac>DfosDN* background, capturing the initial stage of invasion (S1 Movie). The speed of macrophages moving in the area neighboring the germband prior to invasion was not significantly changed (pre-gb, Fig 2B,C). However, the first *mac>DfosDN* macrophage to enter is delayed by 20 min in crossing into the gb (Fig 2D). *mac>DfosDN* macrophages also displayed reduced speed and directional persistence during entering as well as while moving along the first 20μm of the

bioRxiv preprint doi: https://doi.org/10.1101/2020.09.18.301481; this version posted September 18, 2020. The copyright holder for this preprint (which was not certified by peer review) is the author/funder, who has granted bioRxiv a license to display the preprint in perpetuity. It is made available under aCC-BY-NC-ND 4.0 International license.

ectoderm-mesoderm interface (gb entry, Fig 2E, S2A Fig). Macrophages in the *Dfos*^{2} mutant largely mirrored this phenotype, but displayed slower movement in the pre-gb zone neighboring the amnioserosa in which Dfos is also expressed (Fig 1D-F), likely causing a non-autonomous effect (S2B-C Fig, S2 Movie) (Fig 1D, black arrowhead, E-F, white arrowheads). Macrophages expressing DfosDN moved with unaltered average speed as they spread out along the non-invasive route of the vnc (Fig 2F, Fig 2G, S3 Movie), albeit with reduced directional persistence (S2A Fig). We thus conclude from live imaging that Dfos in macrophages aids their initial invasive migration into the gb, increases their speed within the gb and does not underlie their progress along the vnc.

Fig 2. Dfos facilitates the initial invasion of macrophages into the gb tissue

(**A**) Movie stills of control embryos and those expressing DfosDN in macrophages (green, labelled using *srpHemo-H2A::3xmCherry*). Area imaged corresponds to the black dashed square in the schematic above. The germband (gb) border is outlined with a white dashed line. The first entering macrophage is indicated with a white arrowhead, and time in minutes in the upper right corner.

(**B**) Detailed schematic showing the different zones for which the parameters of macrophage gb invasion were quantified. The pre-gb area is shown in yellow, the gb entry zone is outlined in a solid line.

(C) Macrophage speed in the pre-gb area was not significantly changed in macrophages expressing DfosDN (3.00 μm/min) compared to the control (3.61 μm/min), p= 0.58.

(**D**) Quantification shows a 68% increase in the total gb crossing time of DfosDN expressing macrophages compared to the control. Total gb crossing time runs from when macrophages have migrated onto the outer edge of the gb ectoderm, aligning in a half arch, until the first macrophage has translocated its nucleus into the gb ecto-meso interface. p=0.008.

(**E**) DfosDN expressing macrophages displayed a significantly reduced speed (1.53 μm/min) at the gb entry zone compared to the control (1.98 μm/min), p= 1.11e^{-06}.

(**F**) Macrophages expressing DfosDN in a Stage 13 embryo move with unaltered speed along the vnc in the region outlined by the dashed black box in the schematic above (4.93

bioRxiv preprint doi: https://doi.org/10.1101/2020.09.18.301481; this version posted September 18, 2020. The copyright holder for this preprint (which was not certified by peer review) is the author/funder, who has granted bioRxiv a license to display the preprint in perpetuity. It is made available under aCC-BY-NC-ND 4.0 International license.

206 μm/min), compared to the control (4.55 μm/min), p= 0.64. Corresponding stills shown in **(G)**
207 Macrophages are labeled by *srpHemo-Gal4* driving *UAS-GFP::nls*.

208 ***p<0.005, **p<0.01, *p<0.05. Unpaired t-test used for **C-F**, a Kolmogorov-Smirnov test
209 for **D.** For each genotype, the number of tracks analysed in **C** and **F,** and the number of
210 macrophages in **D-E** are indicated within the graph columns. Tracks were obtained from
211 movies of 7 control and 7 *mac>DfosDN* expressing embryos in panel **D**, 3 each in **C, F**, and
212 4 each in **E**. Scale bar: 10 μm.

Dfos modulates Filamin and Tetraspanin to aid gb tissue invasion

213 To identify Dfos targets that promote macrophage invasion, we FACS isolated
214 macrophages from wild type and *mac>DfosDN* embryos during the time when invasion has
215 just begun, and conducted RNA-sequencing of the corresponding transcriptomes (Fig 3A, S1
216 Data). We first assessed reads that map to Dfos, which can correspond to both endogenous
217 and DfosDN mRNA; we found a 1.6 fold increase in the presence of the one copy of DfosDN
218 in this line, arguing that this transgene is expressed at levels similar to each endogenous copy
219 of Dfos and is unlikely to produce extraneous effects (S2 Data). We then examined genes that
220 in the presence of DfosDN displayed a log2 fold change of at least 1.5 with an adjusted P
221 value less than 0.05.10 genes were down-regulated (Fig 3B, S3A-B Fig) and 9 up-regulated
222 by DfosDN (S2 Table). Upregulated genes in DfosDN encoded mostly stress response
223 proteins, so we concentrated on the downregulated class. Of these, we focused on the actin
224 crosslinking filamin Cheerio (Cher) and the tetraspanin TM4SF from a group that can form
225 membrane microdomains that affect signalling and migration (Razinia et al., 2012; Yeung et
226 al., 2018). No known role for TM4SF had been previously identified in *Drosophila*. To
227 determine if these Dfos targets were themselves required for invasion, we RNAi knocked
228 down Cher and TM4SF through RNAi individually or simultaneously and observed
229 significantly reduced macrophage numbers in the gb, particularly upon the knockdown of
230 both targets simultaneously (Fig 3C-G) while not affecting macrophage numbers in the pre-
231 gb zone (S3D Fig) or on the vnc (S3E Fig). Over-expression of Cher or TM4SF along with

bioRxiv preprint doi: https://doi.org/10.1101/2020.09.18.301481; this version posted September 18, 2020. The copyright holder for this preprint (which was not certified by peer review) is the author/funder, who has granted bioRxiv a license to display the preprint in perpetuity. It is made available under aCC-BY-NC-ND 4.0 International license.

DfosDN in macrophages increased the mean macrophage numbers in the gb, and over-expression of TM4SF rescued the *DfosDN* macrophage invasion defect (Fig 3H-L). Expression of a GFP control did not restore macrophage invasion indicating that the rescue we observed through Cher or TM4SF expression was not due to promoter competition leading to reductions in DfosDN expression. We conclude that Dfos aids macrophage gb invasion by increasing the mRNA levels of the filamin actin crosslinker Cher and the tetraspanin TM4SF.

Fig 3. Dfos regulates macrophage germband invasion through cytoskeletal regulators the Filamin Cheerio and the tetraspanin TM4SF

(A) Schematic representing the pipeline for analyzing mRNA levels in FACS sorted macrophages.

(B) Table of genes down-regulated in macrophages expressing DfosDN. Genes are ordered according to the normalized p-value from the RNA-Sequencing. The closest mouse protein orthologs were found using UniProt BLAST; the hit with the top score is shown in the table.

(C-F) Lateral views of representative St 12 embryos in which the two targets with links to actin organization, (**D**) the Tetraspanin TM4SF and (**E**) the Filamin Cheerio, have been knocked down individually or (**F**) together, along with the control (**C**). Scale bar: 50 μm.

(G) Quantification shows that the number of macrophages in the germband is reduced in embryos expressing RNAi against either *cher (KK 107451)* or *TM4SF* (*KK 102206*) in macrophages, and even more strongly affected in the double RNAi of both. Control vs. *cher RNAi* p=0.0005 (46% reduction). Control vs. *TM4SF RNAi* p=0.009 (37% reduction), Control vs. *cher/TM4SF RNAi* p>0.0001 (61% reduction). *cher RNAi* vs. *TM4SF RNAi* p=0.15.

(H-K) Lateral views of a representative St 12 embryo from (**H**) the control, as well as embryos expressing DfosDN in macrophages along with either (**I**) GFP, (**J**) Cher, or (**K**) TM4SF.

(**L**) Quantification shows that over-expression of TM4SF in DfosDN expressing macrophages restores their normal numbers in the gb. Over-expression of Cher in this background shows a strong trend towards rescue, but did not reach statistical significance. Control vs. *DfosDN* p=0.015 (28% reduction); Control vs. *cher* p=0.74; Control vs. *TM4SF*

bioRxiv preprint doi: https://doi.org/10.1101/2020.09.18.301481; this version posted September 18, 2020. The copyright holder for this preprint (which was not certified by peer review) is the author/funder, who has granted bioRxiv a license to display the preprint in perpetuity. It is made available under aCC-BY-NC-ND 4.0 International license.

p>0.99; *DfosDN* vs. *DfosDN cher* p=0.14; DfosDN vs. *DfosDN, TM4SF* p<0.0001; Control vs. *cher* p=0.97; Control vs. *TM4SF* p=0.35.

(M-O) q-PCR analysis of mRNA extracted from the bones of mice that are wild type, transgenic (tg) for *Fos* controlled by a Major Histocompatibility promoter and viral 3'UTR elements, and those in which such c-Fos transgenesis has led to an osteosarcoma (OS). Analysis of mRNA expression shows that higher levels of **(M)** *Fos* correlate with higher levels of **(N-N")** FlnA-C, and **(O)** Tspan6 in osteosarcomas. p values = 0.86, 0.001, 0.003 in **M**, 0.98, 0.009, 0.007 in **N**, 0.39, < 0.0001, <0.0001 in **N'**, 0.76, 0.005, 0.002 in **N"**, 0.99, 0.004, 0.003 in **O**. Scale bar: 50 μm.

Macrophages are labeled using either **(C-F)** *srp::H2A::3xmCherry* or **(H-K)** *srpHemo-Gal4* ("mac>") driving *UAS-mCherry::nls*. ***p<0.005, **p<0.01, *p<0.05. Unpaired t-test or one-way ANOVA with Tukey post hoc were used for statistics. Each column contains the number of analyzed embryos.

In murine osteosarcoma c-fos mRNA level increases correlate with those of Filamins and Tetraspanin-6

To determine if these Dfos targets in *Drosophila* could also be Fos targets in vertebrate cells, we utilized a well-established murine transgenic model that over expresses c-fos. In these mice transgenic c-fos expression from viral 3' UTR elements in osteoblasts (the bone forming cells) leads to osteosarcoma development accompanied by a 5 fold increase in c-fos mRNA expression (Fig 3M) (Linder et al., 2018). We examined by qPCR the mRNA levels of our identified Dfos targets' orthologs, comparing their levels in osteosarcomas (Fos tg OS) to neighboring, osteoblast-containing healthy bones from Fos tg mice (Fos tg bone) and control bones from wild-type mice (wt bone). We saw 2.5 to 8 fold higher mRNA levels of the three murine Filamin orthologs (Fig 3N-N") and a 15 fold increase in Tetraspanin-6 (Fig 3O) in osteosarcoma cells. mRNA levels of several of the orthologs of other Dfos targets we had identified showed less strong inductions or even decreases; the Glutathione S transferase Gstt3 and the Slit receptor Eva1c increased 4 and 2.8 fold respectively, while the mitochondrial translocator Tspo was 25% lower (S3F-I Fig). These results suggest that

bioRxiv preprint doi: https://doi.org/10.1101/2020.09.18.301481; this version posted September 18, 2020. The copyright holder for this preprint (which was not certified by peer review) is the author/funder, who has granted bioRxiv a license to display the preprint in perpetuity. It is made available under aCC-BY-NC-ND 4.0 International license.

289 Dfos's ability to increase mRNA levels of two key functional targets for migration, a
290 Filamin and a Tetraspanin, is maintained by at least one vertebrate fos family member.
291
292 **Dfos increases cortical actin polymerization through Cheerio and TM4SF to aid**
293 **macrophage invasion**
294 We wished to determine what cellular properties Dfos could affect through such targets to
295 facilitate *Drosophila* macrophage invasion. Given Cheerio's known role as an actin
296 crosslinker, we examined actin in invading *mac>DfosDN* macrophages within live embryos.
297 To visualize actin in macrophages, we utilized a *srpHemo-moe::3xmCherry* reporter which
298 marks cortical F-actin (Edwards et al., 1997; Franck et al., 1993) and observed a reduction of
299 53% (Fig 4A-D) in invading m*ac>DfosDN* macrophages. We hypothesized that these
300 changes in actin all around the cell edge could be due to the lower levels of Cheerio and/or
301 TM4SF mRNA in the *mac>DfosDN* macrophages. Indeed, we observed reductions in
302 *moe::3xmCherry* all around the edge of invading macrophages in live embryos expressing
303 RNAi against Cher or TM4SF in macrophages, (Fig 4E-H). To test if a decrease in actin
304 assembly could underlie the reduced tissue invasion of *mac>DfosDN* macrophages, we
305 forced cortical actin polymerization by expressing a constitutively active version of the
306 formin Diaphanous (Dia-CA) which localizes to the cortex (Gonzalez-Gaitan and Peifer,
307 2009). Indeed, Dia-CA completely rescued the *DfosDN* invasion defect (Fig 4I-J). Given that
308 Dia, like Dfos, does not affect general macrophage migratory capacities along the ventral
309 nerve cord (Davis et al., 2015), we examined if Dia might normally play a role in invasion.
310 We utilized two RNAis against Dia and observed decreased macrophage numbers in the gb in
311 each (Fig 4K-L) with no effect on numbers in the pre-gb (S4A Fig) or on the vnc (S4B Fig).
312 These results argue that Dfos aids invasion by increasing levels of TM4SF and Cheerio to

bioRxiv preprint doi: https://doi.org/10.1101/2020.09.18.301481; this version posted September 18, 2020. The copyright holder for this preprint (which was not certified by peer review) is the author/funder, who has granted bioRxiv a license to display the preprint in perpetuity. It is made available under aCC-BY-NC-ND 4.0 International license.

enhance actin polymerization around the surface of the macrophage, potentially by increasing the activity of Dia.

Fig 4. Dfos regulates the actin cytoskeleton through Cher, TM4SF, and the formin Diaphanous

(A) Quantification of phalloidin intensity to detect F actin at the macrophage-macrophage contacts in Stage 11/12 *Dfos*^{1} embryos. F-actin is strongly reduced at these homotypic contacts.

(B-C, F-H) Representative confocal images of live embryos expressing in invading macrophages the F-actin binding and homodimerizing portion of Moesin (*srpHemo-moe::3xmCherry)* to label F-actin. Relative Moe-3xmCherry intensity is indicated with a pseudo-color heat map as indicated on the left, with yellow as the highest levels and dark blue as the lowest.

(D-E) Quantification of the macrophage Moe:3xmCherry intensity as a measure of cortical F-actin, normalized to the average fluorescence intensity of the control per batch.

(D) Quantification shows that macrophages expressing DfosDN display a 53% reduction in Moe::3xmCherry intensity compared to the control when the two outliers shown as single dots are excluded, 37% if they are included. Outliers identified by 10% ROUT. n of ROIs analysed = 650 for control, 687 for *DfosDN*. p=0.0007 for analysis including outliers (Kolmogorov-Smirnov) and p<0.0001 for analysis excluding outliers (Welch's t-test).

(E) Quantification reveals that macrophage expression of an RNAi against either *cher* or *TM4SF*, the two genes whose expression is reduced in *DfosDN*, also results in a decrease of Moe::3xmCherry intensity (by 40% each). n of ROIs analysed = 549 for control, 423 for *cher RNAi,* 306 for *TM4SF RNAi*. Control vs. *cher RNAi* p=0.006. Control vs. *TM4SF* p=0.003.

(I,I') Representative confocal images of St 12 embryos from the control and a line in which macrophages express DfosDN and a constitutively active (CA) form of the formin Dia to restore cortical actin polymerization.

(J) Quantification shows that while macrophage expression of DiaCA does not significantly affect the number of macrophages in the gb, expressing it in a DfosDN background rescues that lines' macrophages gb invasion. Control vs. *DfosDN* p=0.017 (28% reduction), Control vs. *diaCA* p=0.18, Control vs. *DfosDN*, *diaCA* p=0.010, *DfosDN* vs. *DfosDN, diaCA* p<0.0001

(**K,K'**) Representative confocal images of St 12 embryos from the control and from a line expressing an RNAi against *dia* in macrophages.

(L) Quantification of two RNAi lines against *dia* expressed in macrophages shows a 37% and 21% reduction in macrophage numbers in the gb compared to control. Control vs. *dia RNAi*^{1} (TRiP HMS05027) p<0. 0001; control vs. *dia RNAi*^{2} (TRiP HMS00308) p=0.0008.

bioRxiv preprint doi: https://doi.org/10.1101/2020.09.18.301481; this version posted September 18, 2020. The copyright holder for this preprint (which was not certified by peer review) is the author/funder, who has granted bioRxiv a license to display the preprint in perpetuity. It is made available under aCC-BY-NC-ND 4.0 International license.

Macrophages are labeled using either *srpHemo-Gal4* driving *UAS-mCherry::nls* **(I-I')**, or *srpHemo-H2A::3xmCherry* **(K-K')**. *srpHemo-moe::3xmCherry*, *srpHemo-Gal4* crossed to **(B)** *UAS-GFP* as a Control, **(C)** *UAS-DfosDN*, **(F)** w^- Control, **(G)** *UAS-cher RNAi* (KK 107451), or **(H)** *UAS-TM4SF RNAi* (KK 102206). ***p<0.005, **p<0.01, *p<0.05. Unpaired t-test used for **A,** one way ANOVA with Tukey post hoc for **E**, **J, L** and Welch's t test of normalized average mean intensity per embryo for **D** with the two indicated outliers excluded, for statistical assessment. The number of analyzed **(A)** macrophage-macrophage junctions, or **(D-E, J, L)** embryos is shown in each column. Scale bar 10 μm in **(B-C, F-H),** 50 μm in **(I, K).**

We examined what consequence these lower cortical F-actin levels had on the cellular behavior of macrophages during entry. Quantitation showed that the actin protrusion that macrophages initially insert between the ectoderm and mesoderm during invasion was actually longer in the *mac>DfosDN* >LifeAct::GFP macrophages than in the control (Fig 5A, S5A Fig, S4 Movie). We then performed live imaging of macrophages labeled with CLIP::GFP to visualize microtubules and thus cell outlines in both genotypes; we determined the aspect ratio (maximal length over width) that the first entering cell displays as it enters into the gb. The first DfosDN-expressing macrophage was extended even before it had fully moved its rear into the gb (S5B Fig). We carried out measurements, taking only cells that had entered the gb to be able to clearly distinguish the rear of the macrophage from following cells (Fig 5B). We also avoided including in this measurement the forward protrusion and determined that the first macrophage inside the gb displays an average increase of 23% in the maximal length (L) of the cell body and a 12% reduction in the maximal width (W) (S5 Fig). Interestingly, in the pre-gb zone the aspect ratio (max L/W) of *mac>DfosDN* macrophages was not different from control macrophages (Fig 5C-D) although the *mac>DfosDN* cells were 9% smaller in both their length and width (S5D Fig). This suggested that the gb could impose resistance on the entering macrophage, an effect which *mac>DfosDN* macrophages have trouble overcoming due to their compromised actin cytoskeleton at the cortex.

bioRxiv preprint doi: https://doi.org/10.1101/2020.09.18.301481; this version posted September 18, 2020. The copyright holder for this preprint (which was not certified by peer review) is the author/funder, who has granted bioRxiv a license to display the preprint in perpetuity. It is made available under aCC-BY-NC-ND 4.0 International license.

Fig 5. Dfos aids macrophage gb invasion against the resistance of surrounding tissues and buffers the nucleus

(A) Quantification from live embryos shows that the length of the F-actin protrusion of the first entering macrophage is longer in macrophages expressing DfosDN. p= 0.011. The F-actin protrusion labelled with *srpHemo-Gal4* driving *UAS-LifeAct::GFP* was measured in the direction of forward migration (see schematic).

(B-C) Stills from 2-photon movies of St 11 embryos showing **(B)** the first macrophages entering the gb and **(C)** macrophages in the pre-gb zone in the control and in a line expressing DfosDN in macrophages. Microtubules are labelled with *srpHemo-Gal4* driving *UAS-CLIP::GFP*. A blue arrow indicates the front and a yellow arrow indicates the rear of the macrophage. Schematics above indicate where images were acquired

(D) Schematic at left shows macrophage measurements: vertical line for the maximum length and horizontal line for the maximum width. Histograms show the probability density distributions of the aspect ratios (maximum length over maximum width) of the first macrophage entering the gb (left) and macrophages in the pre-gb (right). Macrophages expressing *DfosDN* are more elongated the *mac>DfosDN* line. Control vs. *DfosDN* aspect ratios at gb entry p=0.0004, in pre-gb p=0.39.

Confocal images of St 12 embryos expressing RNAi against Lamin or LaminC in macrophages in **(E-E'')** the control, or **(F-F'')** in embryos also expressing DfosDN in macrophages. *srpHemo-GAL4* used as drover. *Lam RNAi*^{1}: GD45636; *RNAi*^{2}KK107419. *Lam C RNAi:* TRiP JF01406

(G) Macrophage RNAi knockdown of Lamins which can increase nuclear deformability did not affect macrophages numbers in the gb in the control. In embryos in which macrophages expressed DfosDN, Lamin knockdown rescues their reduced numbers in the gb. Control vs. *DfosDN* p<0.0001. Control vs. *Lam RNAi*^{1} p>0.99, vs. *Lam RNAi*^{2} p=0.83, vs. *LamC RNAi* p>0.99. Control vs. *DfosDN, Lam RNAi*^{1} p=0.024, vs. *DfosDN, Lam RNAi*^{2} p>0.99, vs. *DfosDN, LamC RNAi* p>0.99. *DfosDN* vs. *DfosDN, Lam RNAi*^{1} p<0.0001, vs. *DfosDN, Lam RNAi*^{2} p=0.0049, vs. *DfosDN, LamC RNAi* p<0.0001.

(**H**) Expressing *DfosDN* in macrophages reduces their number in the gb. Concomitantly reducing tissue tension in the ectoderm (light blue in schematic) through Rho1DN substantially rescues invasion. *srpHemo-QF QUAS* control (*mac<>)* governed macrophage expression and *e22C-GAL4* ectodermal (*ecto>*). Control vs. *mac<>DfosDN* p<0.0001 (56% reduction), vs. *mac<>DfosDN; ecto>Rho1DN* p>0.99, vs. *ecto>Rho1DN* p=0.11. *mac<>DfosDN* vs. *mac<>DfosDN; ecto>Rho1DN* p<0.0001, vs. *ecto>Rho1DN* p=0.0044. *mac<>DfosDN; ecto>Rh1oDN* vs. *ecto>Rho1DN* p>0.99.

bioRxiv preprint doi: https://doi.org/10.1101/2020.09.18.301481; this version posted September 18, 2020. The copyright holder for this preprint (which was not certified by peer review) is the author/funder, who has granted bioRxiv a license to display the preprint in perpetuity. It is made available under aCC-BY-NC-ND 4.0 International license.

Macrophages are labeled in **B-C** by *srp-Gal4* driving *UAS-CLIP::GFP*, and in **E-F'''** by *srpHemo-Gal4 UAS-mCherry-nls*. ***p<0.005, **p<0.01, *p<0.05. Unpaired t-test was used for **A,** one way ANOVA with Tukey post hoc for **G, H**. The number shown within the column corresponds to measurements in **A,** and analysed embryos in **G, H.** Scale bar 5μm in **B-C**, and 50μm in **E-F**'''.

Dfos promotes advancement of macrophages against the resistance of the surrounding tissues and buffers the nucleus

We therefore examined how the properties of the gb tissues and macrophages interact during invasion. We first investigated if the macrophage nucleus impedes normal invasion by varying levels of the two *Drosophila* Lamin genes, Lam and LamC, both equally related to the vertebrate lamins A and B1 (Muñoz-Alarcón et al., 2007) and both shown to affect nuclear stiffness and deformability (Wintner et al., 2020; Zwerger et al., 2013). Over-expressing Lam (S5E Fig) or knocking down either of these Lamins in macrophages through RNAi (Perkins et al., 2015) did not change macrophage numbers in the gb of wild type embryos (Fig 5E-E''', G), suggesting that the stiffness of the macrophage nucleus is not a rate limiting parameter during normal tissue invasion into the narrow path between the ectoderm and mesoderm, This result also argues that Lamins' capacity to alter gene expression is not normally important for invasion (Andrés & González, 2009). However in *mac>DfosDN* macrophages, knockdown of these Lamins was able to rescue the gb invasion defect (Fig 5E-G), supporting the conclusion that the properties of the nucleus affect invasion in the absence of the higher levels of cortical actin Dfos normally induces. To directly test if reducing the tension of surrounding tissues can counteract the absence of Dfos, we expressed Rho1DN in the ectoderm with the *e22C-GAL4* driver while expressing *QUAS-DfosDN* in macrophages with the GAL4-independent Q-system driver we had constructed, *srpHemo-QF2* (Gyoergy et al., 2018). Rho1 through ROCK is a key regulator of Myosin activity, epithelial tension and tissue stiffness (Warner & Longmore, 2009; Zhou et al., 2009); Myosin II is essential for actin contractility (Heer & Martin, 2017) and tension

bioRxiv preprint doi: https://doi.org/10.1101/2020.09.18.301481; this version posted September 18, 2020. The copyright holder for this preprint (which was not certified by peer review) is the author/funder, who has granted bioRxiv a license to display the preprint in perpetuity. It is made available under aCC-BY-NC-ND 4.0 International license.

in the *Drosophila* gb ectoderm (Ratheesh et al., 2018). Indeed, we found that this reduction of ectodermal tension substantially rescued DfosDN expressing macrophage numbers in the gb (Fig 5H). Taken together our results argue that Dfos aids *Drosophila* macrophages in withstanding the resisting force of surrounding cells against the nucleus during invasion into tissues.

Discussion:

We identify the ability to tune the state of the cortical actin cytoskeleton as a key capacity for immune cells migrating into and within tissue barriers *in vivo*. We find that macrophages upregulate a program governed by the transcription factor Dfos to enable this. Dfos in *Drosophila* is known to regulate the movement during dorsal or wound closure of epithelial sheets (Brock et al., 2012; Lesch et al., 2010; Riesgo-Escovar & Hafen, 1997; Zeitlinger et al., 1997) as well as the development of epithelial tumors and their dissemination (Külshammer et al., 2015; Uhlirova & Bohmann, 2006; Külshammer & Uhlirova, 2013; Benhra et al., 2018). Here we define a different role, namely that Dfos enables a stream of individual immune cells to efficiently push their way into tissues, a process which is aided rather than hampered by the presence of the ECM (Sánchez-Sánchez et al., 2017; Valoskova et al., 2019). This function appears specifically required for invasion as we observe no defects in *DfosDN* macrophages' migratory speed in open environments. *DfosDN* macrophages display decreased actin at the cell edge and an elongated shape within the germband, suggesting a defect in the stiffness of the cortex. Indeed, only in the presence of *DfosDN* does the state of the nucleus become relevant, with reductions in Lamins shown to underlie nuclear stiffness (Wintner et al., 2020) enhancing the ability of macrophages to invade. These findings along with the ability of a softened ectoderm to substantially rescue the *DfosDN* macrophages' germband invasion defect lead us to propose the model (Fig 6)

bioRxiv preprint doi: https://doi.org/10.1101/2020.09.18.301481; this version posted September 18, 2020. The copyright holder for this preprint (which was not certified by peer review) is the author/funder, who has granted bioRxiv a license to display the preprint in perpetuity. It is made available under aCC-BY-NC-ND 4.0 International license.

that Dfos permits efficient initial translocation of the macrophage body under ectodermal reactive load by forming a stiff cortical actin shell that counteracts surrounding tissue resistance and protects the nucleus from undergoing high levels of mechanical stress during its deformation.

Fig. 6. Model: Dfos increases actin assembly and crosslinking through the tetraspanin TM4SF and the Filamin Cheerio to counter surrounding tissue resistance

We propose a model for how Dfos tunes the cortical actin properties of *Drosophila* embryonic macrophages to aid their infiltration against the resistance of the surrounding germband tissue. Dfos leads to an increase of the tetraspanin TM4SF and the Filamin Cheerio (Cher). The binding of TM4SF and Filamin to different partners (see Figure S6) forms a network at the cell surface of Integrin, actin and upstream signaling molecules; this results in the recruitment of Rho GEFs and activation of Rho GTPases and the formin Diaphanous, which can stimulate further actin polymerization. Thereby, F-actin is assembled into a more crosslinked and dense network aiding the macrophage in moving its cell body into the ecto-meso interface. The presence of Lamin around the nuclear membrane does not affect this process in the wildtype. However, in the DfosDN-expressing macrophages, the loss of Cher and TM4SF lead to reduced cross-linked actin levels at the cell cortex making the stiffness of the nucleus the rate limiting step for macrophage infiltration of the gb tissue.

A molecular program for tissue invasion that strengthens cortical actin

Crucial mediators of this process are two actin regulators, the filamin Cher, known to be a Dfos target in epithelia, and the previously uncharacterized membrane scaffold tetraspanin TM4SF. We show that both require Dfos for higher mRNA levels in macrophages and present correlative evidence that these classes of genes are also upregulated by vertebrate c-fos. Each of these Dfos targets is required for macrophage invasion; over-expression of TM4SF in macrophages can rescue the *DfosDN* tissue invasion phenotype. We propose that these targets act together to tune the actin cytoskeleton for tissue invasion. Higher Filamin levels cross-link actin filaments into resilient and stiffer networks maintaining cell integrity during mechanical stress (Goldmann et al., 1997; Tseng et al., 2004; Fujita et al., 2012). This aids the distribution of forces from focal adhesions

bioRxiv preprint doi: https://doi.org/10.1101/2020.09.18.301481; this version posted September 18, 2020. The copyright holder for this preprint (which was not certified by peer review) is the author/funder, who has granted bioRxiv a license to display the preprint in perpetuity. It is made available under aCC-BY-NC-ND 4.0 International license.

485 across the entire migrating cell body, since Filamins can bind directly to Integrin, and even
486 more strongly under strain (Ehrlicher et al., 2011; Glogauer et al., 1998; Kumar et al., 2019;
487 Razinia et al., 2012). Tetraspanins, self-associating multipass transmembrane proteins, also
488 can bind Integrin, forming microdomains of adhesion molecules, receptors and their
489 intracellular signaling complexes, including Rho GTPases (Zimmerman, et al., 2016;
490 Termini & Gillette, 2017; Yáñez-Mó et al., 2009; Berditchevski & Odintsova, 1999).
491 Filamins similarly bind receptors, regulators of actin assembly, Rho GTPases and the Rho
492 GEF Trio (Popowicz et al., 2006; Stossel et al., 2001; Vadlamudi et al., 2002; Ohta et al.,
493 1999; Bellanger et al., 2000). Given that we observe reduced macrophage cortical F-actin in
494 the absence of either the Filamin Cheerio or the Tetraspanin TM4SF we propose that these
495 targets enhance the recruitment and activation of Rho GTPases and the formin Dia to
496 stimulate actin polymerization (Fig 6, S6 Fig) (Rousso et al., 2013; Seth et al., 2006;
497 Großhans et al., 2005; Williams et al., 2007; Delaguillaumie et al., 2002). Dfos'
498 upregulation of both targets could thus lead to a supra-network in which ECM-anchored FAs
499 connect to a strong cross-linked cortical actin lattice, allowing Myosin contraction to be
500 converted into cellular advancement despite resistance from the flanking ectoderm.

501 We demonstrate that the actin nucleating formin Dia is important for *Drosophila*
502 macrophage invasion and capable of rescuing the defects in the *DfosDN* mutant. Unlike the
503 formin Ena which mediates chemotaxis (Davidson et al., 2019), Dia is not required for
504 general *Drosophila* macrophage migration, and instead allows macrophages to recoil away
505 from one another (Davis et al., 2015). Dia could be required for macrophages specifically
506 when they face resistance from their surroundings. Modeling indicates that Dia1's regulation
507 of cortical tension requires an optimal combination of actin cross linking and intermediate
508 actin filament length (Chugh et al., 2017). *Drosophila* Dia is a more processive nucleator
509 than Ena (Bilancia et al., 2014) and thus could create the intermediate length actin filaments

bioRxiv preprint doi: https://doi.org/10.1101/2020.09.18.301481; this version posted September 18, 2020. The copyright holder for this preprint (which was not certified by peer review) is the author/funder, who has granted bioRxiv a license to display the preprint in perpetuity. It is made available under aCC-BY-NC-ND 4.0 International license.

that enable higher levels of macrophage cortical tension and strain stiffening (Kasza et al., 2010) on all sides of the cell during their invasion.

Our findings thus demonstrate that there are commonalities in the molecular mechanisms by which *Drosophila* cells invade into either confluent tissues or the ECM. Dfos's upregulation of the Filamin Cheerio is also required in tumor cells and aneuploid epithelial cells to enhance ECM breaching (Külshammer & Uhlirova, 2013; Benhra et al., 2018). Both cell types displayed enhanced levels of cortical filamentous actin, which in the tumors is concomitant with Dia upregulation (Külshammer & Uhlirova, 2013). In the oocyte, Filamin is required for follicle cell intercalation and border cells display higher levels of Filamin and F-actin to maintain cellular integrity during migration between nurse cells (Sokol & Cooley, 2003; Somogyi & Rørth, 2004). The mediator of these increased F-actin levels, MAL-D, can be activated by Dia (Somogyi & Rørth, 2004). Thus while MMPs may be specific to ECM crossing, a denser and more cross linked actin cortex due to increased levels of the filamin Cheerio and activity of the formin Dia could be a common feature of *Drosophila* cells moving through the resistance of either ECM or surrounding tissues. Determining if such shifts in cell surface actin properties underlie some cancer cells' capacity to metastasize even in the presence of MMP inhibitors is an interesting area of inquiry (Butcher et al 2009; Kessenbrock et al 2010).

Implications for vertebrate immune cell migration

Our work also suggests a new perspective on the migration of some vertebrate immune cells. We find that altering lamin levels does not normally affect *Drosophila* macrophage tissue invasion. This contrasts with results showing that nuclear deformability from lower lamin levels underlies the migration of some immune cell types through narrow constrictions engineered from rigid materials (Davidson et al., 2014; Thiam et al, 2016).

bioRxiv preprint doi: https://doi.org/10.1101/2020.09.18.301481; this version posted September 18, 2020. The copyright holder for this preprint (which was not certified by peer review) is the author/funder, who has granted bioRxiv a license to display the preprint in perpetuity. It is made available under aCC-BY-NC-ND 4.0 International license.

535 However, negotiation of such extremely challenging *in vitro* environments can lead to DNA
536 damage (Raab et al., 2016) and higher nuclear flexibility caused by lower lamin levels is
537 associated with increased cell death (Harada et al., 2014). A robust cell surface actin layer
538 would allow long-lived cells or those not easily replenished to protect their genome as they
539 move through resistant yet deformable environment. Embryonic *Drosophila* and vertebrate
540 tissue resident macrophages migrate into tissues during development, survive into the adult,
541 and serve as founders of proliferative hematopoetic niches (Holz et al., 2003; Makhijani et
542 al., 2011; Bosch et al., 2019; Ginhoux and Guilliams, 2016; Theret et al 2019; Guilliams et
543 al, 2020). Tissue resident memory T cells migrate in response to infection in mature animals,
544 are long-lived and not easily renewed from the blood (Szabo et al., 2019). Thus the
545 importance of nuclear mechanics for migration in challenging *in vivo* environments should
546 be explored for a broader range of immune cells as well as the utilization of cortical actin as
547 a strategy for genomic protection.
548
549

550 # Materials and Methods

551 ## Fly strains and genetics

552 Flies were raised on standard food bought from IMBA (Vienna, Austria) containing agar,
553 cornmeal, and molasses with the addition of 1.5% Nipagin. Adults were placed in cages in a
554 fly room or a Percival DR36VL incubator maintained at 25ºC and 65% humidity or a Sanyo
555 MIR-153 incubator at 29ºC within the humidity controlled 25ºC fly room; embryos were
556 collected on standard plates prepared in house from apple juice, sugar, agar and Nipagin
557 supplemented with yeast from Lesaffre (Marcq, France) on the plate surface. Fly crosses and
558 embryo collections for RNA interference experiments (7 hour collection) as well as live

bioRxiv preprint doi: https://doi.org/10.1101/2020.09.18.301481; this version posted September 18, 2020. The copyright holder for this preprint (which was not certified by peer review) is the author/funder, who has granted bioRxiv a license to display the preprint in perpetuity. It is made available under aCC-BY-NC-ND 4.0 International license.

559 imaging (6 hour collection) were conducted at 29ºC to optimize expression under GAL4
560 driver control (Duffy, 2002). All fly lines utilized are listed below.
561
562 **Fly stocks**
563 *srpHemo-GAL4 (mac>)* was provided by K. Brückner (UCSF, USA)(Brückner et al., 2004).
564 *Oregon R (control), P{CaryP}attP2 (control), P{CaryP}attP40 (control), kay^{2} (Dfos^{2}),*
565 *(UAS-Fra)2 (Dfos), UAS-Rho1.N19 Rho1DN), UAS-fbz (DfosDN), UAS-kayak* RNAi *(Dfos*
566 *RNAi)* TRiP HMS00254 and TRiP JF02804, *UAS-dia RNAi* TRiP HM05027, *UAS-LamC*
567 *RNAi* TRiP JF01406 and TRiP HMS00308, *e22c-GAL4 (ecto>)*, *Resille::GFP*, *UAS-*
568 *GFP.nls, UAS-mCherry.nls, UAS-CD8::GFP* lines were obtained from the Bloomington
569 Stock Center (Indiana, USA). *kay^{1}* (*Dfos^{1})* line was provided by O. Schuldiner (WIS, Israel).
570 *UAS-dia.deltaDad.EGFP (diaCA)* and *srpHemo-GAL4 UAS-CLIP::GFP*
571 *(mac>CLIP::GFP)* lines were provided by B. Stramer (KCL, UK). *UAS-cher.FLAG (cher)*
572 line was provided by M. Uhlirova (CECAD, Germany). *w[1118] (control), UAS-cher* RNAi
573 KK107451, *UAS-TM4SF* RNAi KK102206, *UAS-Lam RNAi^{1}* GD45636, *UAS-Lam RNAi^{2}*
574 KK107419 lines were obtained from the Vienna *Drosophila* Resource Center (Austria).
575 **Extended genotypes:**
576 Here we list the lines used in each Fig; we state first the name from FlyBase; in parentheses
577 the name used in the Fig panels is provided.
578 **Fig 1 and S1 Fig:**
579 Fig 1D: *Oregon R*. Fig 1E-G and S1A Fig: *srpHemo-GAL4, UAS-GFP (control)*. Fig 1H:
580 *srpHemo-GAL4, UAS-GFP; kay^{1} (Dfos^{1})*. Fig 1I-L and S1B, G Fig: *srpHemo-GAL4, UAS-*
581 *GFP.nls/+ (control 1)*. Fig 1H, 1J, 1N: *srpHemo-GAL4, UAS-GFP/+; kay^{1} (Dfos^{1})*. Fig 1K, 1N
582 and S1B Fig: *srpHemo-GAL4, UAS-GFP.nls/+; kay^{2} (Dfos^{2})* Fig 1L, 1N: *srpHemo-GAL4, UAS-*
583 *GFP.nls/(UAS-Fra)2*; *kay^{2} (Dfos^{2};mac>Dfos)*. Fig 1O, 1Q and S1C-E Fig: *srpHemo-Gal4,*

bioRxiv preprint doi: https://doi.org/10.1101/2020.09.18.301481; this version posted September 18, 2020. The copyright holder for this preprint (which was not certified by peer review) is the author/funder, who has granted bioRxiv a license to display the preprint in perpetuity. It is made available under aCC-BY-NC-ND 4.0 International license.

584 *srpHemo-H2A::*3x*mCherry/+ (control 2)*. Fig 1P-Q and S1C-E Fig: *srpHemo-Gal4, srpHemo-*
585 *H2A::*3x*mCherry/UAS-fbz (mac>DfosDN)*. Fig 1R and S1F Fig: *srpHemo-GAL4, UAS-GFP,*
586 *UAS-H2A::RFP/ P{CaryP}attP2 (control)*. Fig 1R and S1F Fig: *srpHemo-GAL4, UAS-GFP,*
587 *UAS-H2A::RFP /UAS-kayak* RNAi HMS00254 and JF02804 (*mac>Dfos RNAi*^{1}, *mac>Dfos*
588 *RNAi*^{2}). S1G Fig: *srpHemo-GAL4, UAS-GFP.nls/(UAS-Fra)2 (mac>Dfos)*.

589 **Fig 2 and S2 Fig:**

590 Fig 2A, 2C-I and S2A-B, E Fig: *srpHemo-Gal4, srpHemo-H2A::*3x*mCherry/+ (control)*. Fig
591 2D: *srpHemo-Gal4, srpHemo-H2A::*3x*mCherry/+* (3 movies) and *Resille::GFP/+; srpHemo-*
592 *Gal4, srpHemo-H2A::*3x*mCherry/+* (4 movies, control) and *Resille::GFP/+; srpHemo-Gal4,*
593 *srpHemo-H2A::*3x*mCherry/+* (3 movies) and *Resille::GFP/+; srpHemo-Gal4, srpHemo-*
594 *H2A::*3x*mCherry/UAS-DfosDN (*4 movies, *DfosDN)* Fig 2A, 2C-I and S2A-B, E Fig: *srpHemo-*
595 *Gal4, srpHemo-H2A::*3x*mCherry/UAS-fbz (mac>DfosDN)*. S2C-D Fig: *srpHemo-GAL4, UAS-*
596 *GFP.nls/+ (control)*. S2C-D Fig: *srpHemo-GAL4, UAS-GFP.nls/+; kay*^{2} *(Dfos*^{2}*)*.

597 **Fig 3 and S3 Fig:**

598 Fig 3C, G and S3D Fig: *UASDicer2;; srpHemo-Gal4, srpHemo-H2A::*3x*mCherry/w*^{1118}
599 *(control)*. Fig 3D, 3G and S3D Fig: *UASDicer2; UAS-TM4SF RNAi* KK10220/*+; srpHemo-*
600 *Gal4, srpHemo-H2A::*3x*mCherry/+ (mac>TM4SF RNAi)*. Fig 3E, G and S3D Fig:
601 *UASDicer2; UAS-cher RNAi* KK107451/*+; srpHemo-Gal4, srpHemo-H2A::*3x*mCherry/+*
602 *(mac>cher RNAi)*. Fig 3F-G: *UAS-Dicer2;UAS-cher RNAi* KK107451/*UAS-TM4SF RNAi*
603 KK102206; *srpHemo-Gal4, srpHemo-H2A::*3x*mCherry/+ (mac>TM4SF RNAi, cher RNAi)*.
604 Fig 3H, L: *srpHemo-GAL4, UAS-mCherry.nls/UAS-mCD8::GFP (control)*. Fig 3I, L:
605 *srpHemo-GAL4, UAS-mCherry.nls/UAS-mCD8::GFP; UAS-fbz/+ (mac>DfosDN)*. Fig 3J,
606 L: *srpHemo-GAL4,UAS-mCherry.nls/UAS-cheerio.FLAG; UAS-fbz/+ (mac>DfosDN, cher)*.
607 Fig 3K-L: *srpHemo-GAL4,UAS-mCherry.nls/UAS-TM4SF; UAS-fbz/+ (mac>DfosDN,*
608 *TM4SF)*. Fig 3L: *srpHemo-GAL4, UAS-mCherry.nls/ UAS-TM4SF (mac>TM4SF)*. Fig 3L:

bioRxiv preprint doi: https://doi.org/10.1101/2020.09.18.301481; this version posted September 18, 2020. The copyright holder for this preprint (which was not certified by peer review) is the author/funder, who has granted bioRxiv a license to display the preprint in perpetuity. It is made available under aCC-BY-NC-ND 4.0 International license.

srpHemo-GAL4, UAS-mCherry.nls/ UAS-cher (mac>cher). S3A-C Fig: *srpHemo-Gal4, srpHemo-*3x*mCherry/+ (control)*. S3A-C Fig: *srpHemo-Gal4, srpHemo-*3x*mCherry/UAS-fbz (mac>DfosDN)*.

Fig 4 and S4 Fig:

Fig 4B, D: *srpHemo-Gal4, srpHemo-moe::*3x*mCherry/+;UAS-mCD8::GFP/+ (Control)*. Fig 4C-D: *srpHemo-Gal4, srpHemo-moe::*3x*mCherry/UAS-fbz (mac>DfosDN)*. Fig 4E-F: *srpHemo-Gal4, srpHemo-moe::*3x*mCherry/w118 (Control)*. Fig 4E, G: *srpHemo-Gal4, srpHemo-moe::*3x*mCherry/UAS>cher RNAi* KK107451 *(mac>cher RNAi)*. Fig 4E, H: *srpHemo-Gal4, srpHemo-moe::*3x*mCherry/UAS>TM4SF RNAi* KK102206 *(mac>TM4SF RNAi)*. Fig 4I-J: *srpHemo-GAL4, UAS-mCherry.nls/UAS-mCD8::GFP (control)*. Fig 4I', J: *srpHemo-GAL4, UAS-mCherry.nls/UAS-Dia.deltaDad.EGFP; UAS-fbz/+ (mac> DfosDN, diaCA)*. Fig 4J: *srpHemo-GAL4, UAS-mCherry.nls/UAS-mCD8::GFP; UAS-fbz/+ (mac>DfosDN)*. Fig 4J: *srpHemo-GAL4, UAS-mCherry.nls/ UAS-Dia.deltaDad.EGFP (mac>diaCA)*. Fig 4K-L and S4B-C Fig: *UASDicer2;; srpHemo-Gal4, srpHemo-H2A::*3x*mCherry/P{CaryP}attP40 (control)*. Fig 4K', L and S4B-C Fig: *UASDicer2;+; srpHemo-Gal4, srpHemo-H2A::*3x*mCherry/ UAS-dia RNAi* HM05027 *(mac>dia RNAi*^{1}*)*. Fig 4L and S4B-C Fig: *UASDicer2;+; srpHemo-Gal4, srpHemo-H2A::*3x*mCherry/UAS-dia RNAi* HMS00308 *(mac>dia RNAi*^{2}*)*.

Fig 5 and S5 Fig:

Fig 5A and S5A Fig: *srpHemo-Gal4 UAS-LifeActGFP UAS-RedStinger/ srpHemo-Gal4 UAS-LifeActGFP, UAS-RedStinger* control*; srpHemo-Gal4 UAS-LifeActGFP UAS-RedStinger/ srpHemo-Gal4 UAS-LifeActGFP UAS-RedStinger; UAS-DfosDN/UAS-DfosDN*. Fig 5B-D and S5B-D Fig: *srpHemo-Gal4, UAS-CLIP::GFP, UAS-RedStinger (control)*. Fig 5B-D and S5B-D Fig: *srpHemo-Gal4, UAS-CLIP::GFP, UAS-RedStinger; UAS-fbz*

bioRxiv preprint doi: https://doi.org/10.1101/2020.09.18.301481; this version posted September 18, 2020. The copyright holder for this preprint (which was not certified by peer review) is the author/funder, who has granted bioRxiv a license to display the preprint in perpetuity. It is made available under aCC-BY-NC-ND 4.0 International license.

(mac>DfosDN). Fig 5E, G: *srpHemo-GAL4, UAS-mCherry.nls/UAS-mCD8::GFP (control)*. Fig 5E'-E'', 5G: *srpHemo-GAL4, UAS-mCherry.nls/UAS-Lamin RNAi* GD45636, KK107419 *(mac>Lam RNAi^{1}* and *mac>Lam RNAi^{2}, respectively)*. Fig 5E''', G: *srpHemo-GAL4, UAS-mCherry.nls/UAS-LaminC RNAi* TRIP JF01406 *(mac>LamC RNAi)*. Fig 5F-G: *srpHemo-GAL4, UAS-mCherry.nls/UAS-mCD8::GFP; UAS-fbz/+ (mac>DfosDN)*. Fig 5F',F'', G: *srpHemo-GAL4, UAS-mCherry.nls/UAS-Lam RNAi* (*Lam RNAi^{1}*=GD45636, *Lam RNAi^{2}*=KK107419)*; UAS-fbz/+ (mac>DfosDN, Lam RNAi^{1}* and *mac>DfosDN, Lam RNAi^{2})*. Fig 5F''', G: *srpHemo-GAL4, UAS-mCherry.nls/UAS-LaminC RNAi* TRIP JF01406*; UAS-fbz/+ (mac>DfosDN, LamC RNAi)*. Fig 5H: *e22CGal4,srpHemo-H2A::*3x*mCherry/+ (control)*. Fig 5H: *srpQF/ srpHemo-H2A::*3x*mCherry; QUAS-fbz/UAS-Rho1.N12 (mac<>DfosDN)*. Fig 5H: *e22CGal4, srpHemo-H2A::*3x*mCherry/srpQF; +/ UAS-Rho1.N12 (ecto>Rho1DN)*. Fig 5H: *srpQF/ e22C-Gal4, srpHemo-H2A::*3x*mCherry; UAS-Rho1N12/QUAS-fbz (mac<>DfosDN, ecto>rhoDN)*. S5E Fig: *+;UAS-GFP::nls, srpHemo-GAL4 (control). +;UAS-GFP::Lamin, srpHemo-GAL4.*

Cloning and generation of QUAS-DfosDN line

The fragment was amplified from genomic DNA of the published *UAS-fbz (UAS-Dfos DN)* line (Eresh, Riese, Jackson, Bohmann, & Bienz, 1997) using primers encompassing a 5' consensus translation initiation sequence followed by the bZIP fragment and containing BglII and XhoI restriction sites: 5'-GAAGATCTATTGGGAATTCAACATGACCCCG-3' and 5'-CCCTCGAGTCAGGTGACCACGCTCAGCAT-3'. The resulting fragment was cloned into the pQUASt vector, a gift from Christopher Potter (Addgene plasmid # 104880). The final construct was sequenced and injected into the attP2 landing site by BestGene (Chino Hills, CA, USA).

bioRxiv preprint doi: https://doi.org/10.1101/2020.09.18.301481; this version posted September 18, 2020. The copyright holder for this preprint (which was not certified by peer review) is the author/funder, who has granted bioRxiv a license to display the preprint in perpetuity. It is made available under aCC-BY-NC-ND 4.0 International license.

659 **Cloning and generation of UAS-TM4SF line**

660 The TM4SF open reading frame was amplified from the DGRC GH07902 cDNA clone
661 (#3260, Fbcl0121651), using primers acagcgGAATTCATGGCATTGCCGAAGAAAAT
662 and acagcgTCTAGATTAAAAGCTAATCGTCTGTCATT. The PCR product and the
663 pUASt-aTTB vector (DGRC plasmid #1419) were digested with EcoRI and XbaI, and
664 ligated. After sequencing, the construct was injected into the landing site line, (y^1 *M{vas-*
665 *int.Dm}ZH-2A w**; *M{3xP3-RFP.attP}ZH-51D*, BL 24483), to produce second chromosome
666 inserts. All male survivors were crossed to *w*; *Sp/CyO*; *PrDr/TM3Ser* virgins. Transformants
667 were recognized by eye color and crossed again to *w*; *Sp/CyO*; *PrDr/TM3Ser* virgins to get
668 rid of the X chromosomal integrase.

669

670 **Embryo staging:**

671 Laterally oriented embryos with complete germband (gb) extension and the presence of
672 stomadeal invagination were staged based on gb retraction from the anterior as a percentage
673 of total embryo length. Embryos with no gb retraction were classified as Stage 11, 30%
674 retraction early Stage 12, 60% retraction Stage 12, and 70% Stage 13. Imaged embryos are
675 shown throughout paper in a lateral orientation with anterior to the left and dorsal up.

676

677 ***In situ* hybridization and immunofluorescence**

678 Embryos were fixed with 3.7% formaldehyde/heptane for 20 min followed by methanol
679 devitellinization for *in situ* hybridization and visualization of 3xmCherry. The *Dfos* cDNA
680 clone SD04477 was obtained from the DGRC. T7 or T3 polymerase-synthesized
681 digoxigenin-labelled anti-sense probe preparation and *in situ* hybridization was performed
682 using standard methods (Lehmann & Tautz, 1994). Images were taken with a Nikon-Eclipse
683 Wide field microscope with a 20X 0.5 NA DIC water Immersion Objective. Embryos were

bioRxiv preprint doi: https://doi.org/10.1101/2020.09.18.301481; this version posted September 18, 2020. The copyright holder for this preprint (which was not certified by peer review) is the author/funder, who has granted bioRxiv a license to display the preprint in perpetuity. It is made available under aCC-BY-NC-ND 4.0 International license.

684 mounted after immunolabeling in Vectashield Mounting Medium (Vector Labs, Burlingame,
685 USA) and imaged with a Zeiss Inverted LSM700 and LSM800 Confocal Microscope using a
686 Plain-Apochromat 20X/0.8 Air Objective or a Plain-Apochromat 63X/1.4 Oil Objective as
687 required.

Antibody	Source animal	Dilution	Provided by
Anti-Dfos	Rabbit	1:50	J. Zeitlinger (Stowers Institute, USA)
Anti-GFP	Chicken	1:500	Abcam (ab13970)
Anti-mCherry	Goat	1:200	Invitrogen (M11217)

688

689 **Dfos antibody**

690 The Dfos rabbit polyclonal antibody was produced for the lab of Julia Zeitlinger. It was
691 raised by Genescript (Piscataway, NJ, USA) against the C-terminal end of *Drosophila* Kayak
692 found in all isoforms and was purified against an N terminally His tagged antigen
693 corresponding to aa 73 to 595 of Kay isoform A. The internal Genescript order number is
694 163185-30, and in the Zeitlinger lab is referred to as anti-kay/fos Ab.

695

696 **Time-Lapse Imaging**

697 Embryos were dechorionated in 50% bleach for 5 min, washed with water, and mounted in
698 halocarbon oil 27 (Sigma) on a 24x50mm high precision coverslip (Marienfeld Laboratory
699 Glassware, No. 1.5H) between two bridges (~0.5 cm high) of coverslips glued on top of
700 each other, or mounted in halocarbon oil 27 (Sigma) between a 18x18mm coverslip
701 (Marienfeld Laboratory Glassware, No. 1.5H) and an oxygen permeable membrane (YSI).
702 The embryo was imaged on an upright multiphoton microscope (TrimScope, LaVision)
703 equipped with a W Plan-Apochromat 40X/1.4 oil immersion objective (Olympus). GFP and
704 mCherry were imaged at 860 nm and 1100 nm excitation wavelengths, respectively, using a
705 Ti-Sapphire femtosecond laser system (Coherent Chameleon Ultra) combined with optical
706 parametric oscillator technology (Coherent Chameleon Compact OPO). Excitation intensity

bioRxiv preprint doi: https://doi.org/10.1101/2020.09.18.301481; this version posted September 18, 2020. The copyright holder for this preprint (which was not certified by peer review) is the author/funder, who has granted bioRxiv a license to display the preprint in perpetuity. It is made available under aCC-BY-NC-ND 4.0 International license.

profiles were adjusted to tissue penetration depth and Z-sectioning for imaging was set at 1µm for tracking. For long-term imaging, movies were acquired for 60 - 150 minutes with a frame rate of 25-45 seconds. A temperature control unit set to 29°C was utilized for all genotypes except *kay*^{2} for which the setting was 25°C.

Image Analysis

Macrophage cell counts: Autofluorescence of the embryo revealed the position of the germband (gb) for staging of fixed samples. Embryos with 40% (±5%) gb retraction (Stage 12) were analysed for macrophage numbers in the pre-gb, within the germband, along the ventral nerve cord (vnc) and in the whole embryo. For the *kay RNAi*.embryos with 70% gb retraction (Stage 13) were used for vnc counts. The pre-gb zone was defined based on embryo and yolk autofluorescence as an area on the yolk sac underneath the amnioserosa with borders defined posteriorly by the gb ectoderm and anteriorly by the head. Macrophages were visualized using confocal microscopy with a Z-stack step size of 2 µm and macrophage numbers within the gb or the segments of the vnc were calculated in individual slices (and then aggregated) using the Cell Counter plugin in FIJI. Total macrophage numbers were obtained using Imaris (Bitplane) by detecting all the macrophage nuclei as spots.

Macrophage Tracking, Speed, Persistence. Mode of Migration and Macrophage gb crossing Analysis

Embryos with macrophage nuclei labelled with *srpHemo-H2A::3XmCherry* and the surrounding tissues with *Resille::GFP,* or with only macrophages labelled by *srpHemo-H2A::3XmCherry, or srpHemo>GFP.nls* were imaged and 250x250x40µm^{3} 3D-stacks were typically acquired with ~0.2x0.2x1µm^{3} voxel size every 39-41 seconds for ~2 hours. For

bioRxiv preprint doi: https://doi.org/10.1101/2020.09.18.301481; this version posted September 18, 2020. The copyright holder for this preprint (which was not certified by peer review) is the author/funder, who has granted bioRxiv a license to display the preprint in perpetuity. It is made available under aCC-BY-NC-ND 4.0 International license.

imaging macrophages on vnc frames were acquired at every 40-43 seconds for 30 min after macrophages started spreading into abdominal segment 2 (see Fig 2G). Multiphoton microscopy images were initially processed with ImSpector software (LaVision Bio Tec) to compile channels, and exported files were further processed using Imaris software (Bitplane) for 3D visualization.

Each movie was rotated and aligned along the embryonic AP axis for tracking analysis. For analysis of migration in the pre-gb and gb in the control and *kay*^{2} mutant, embryos were synchronized using the onset of germ and retraction. For vnc migration analysis, macrophages were tracked for 30 minutes from when macrophages started moving into the second abdominal segment. Only macrophages migrating along the inner edge of the vnc were analyzed.

Gb crossing time was calculated from when the macrophages align in front of the gb ectoderm in a characteristic arc, until the first macrophage had transitioned its nucleus inside the ecto-meso-interphase. To see the gb edge and yolk in movies of *srpHemo-3xH2A::mCherry*, either *Resille::GFP* labelling the outlines of all cells, or the auto-fluorescence of the yolk was used.

For analysis of gb migration in the *DfosDN* vs control macrophages, macrophages were tracked from when the first macrophage appeared between the ectoderm and the yolk sac until gb retraction started, typically 60 minutes. In the head and pre-gb, macrophage nuclei were extracted using the spot detection function, and tracks generated in 3D over time. The pre-gb and gb were defined as for macrophage counts described above. The mean position of the tracks in X- and Y restrict analysis to each migratory zones.

Cell speed and persistence were calculated from nuclei positions using custom Python scripts as described elsewhere (Smutny et al., 2017). Briefly, instantaneous velocities from single cell trajectories were averaged to obtain a mean instantaneous velocity value over the

bioRxiv preprint doi: https://doi.org/10.1101/2020.09.18.301481; this version posted September 18, 2020. The copyright holder for this preprint (which was not certified by peer review) is the author/funder, who has granted bioRxiv a license to display the preprint in perpetuity. It is made available under aCC-BY-NC-ND 4.0 International license.

course of measurement. The directional persistence of a trajectory was calculated as the mean cosine of an angle between subsequent instantaneous velocities:

$$I\,(v_1, \ldots, v_l) = \frac{1}{l-1}\sum_{k=1}^{l-1} \cos(v_k, v_{k+1}),$$

where l is duration of the trajectory and $v_1, \ldots, v_l$ are its instantaneous velocities. Only trajectories with a minimal duration of 15 timeframes were used. Calculated persistence values were averaged over all trajectories to obtain a persistence index (I) for the duration of measurement (with -1 being the lowest and 1 the maximum). 3-6 embryos were recorded and analyzed for each genotype, numbers of control and perturbed embryos are equal in each pairwise comparison.

Measurement of junctional Phalloidin

The junctional intensity of F-actin (Phalloidin) was calculated using linescan analysis as previously described (Smutny et al., 2010) with the following changes. The line was ~5 µm and was always drawn in the middle slice of the Z stack (1 µm resolution) of the macrophage-macrophage junction. For every line, a Gaussian fit was applied and maximum intensities across the cell junction were then normalized against average intensities of F-actin (Phalloidin) staining in the stereotypical gb area of ~50x50µm^2 in each embryo. Analyses were carried out using standard Fiji software. 4-5 embryos were analysed per genotype. Macrophages in the pre-gb or gb entry zones were analyzed.

Measurement of F-actin reporters

To quantify cortical F-actin intensity in living embryos, a *srpHemo-moe::3xmCherry* reporter line (Gyoergy et al., 2018) was crossed into a background of macrophages expressing *DfosDN*, *cher RNAi*, or *TM4SF* RNAi. Embryos were collected for 5h 30min at

bioRxiv preprint doi: https://doi.org/10.1101/2020.09.18.301481; this version posted September 18, 2020. The copyright holder for this preprint (which was not certified by peer review) is the author/funder, who has granted bioRxiv a license to display the preprint in perpetuity. It is made available under aCC-BY-NC-ND 4.0 International license.

29°C, de-chorionated in 50% bleach for 5 min, rinsed thoroughly with water, and aligned laterally side by side under a stereomicroscope using a fluorescence lamp to check for the presence of mCherry. Aligned embryos were then mounted as described in the live imaging section above. To image Moe::3xmCherry, a Zeiss LSM800 inverted microscope was used with the following settings: Plan-APOCHROMAT 40x/1.4 Oil, DIC, WD=0.13 objective, 1.5x zoom, 1025x1025 pixel, speed 8, heating chamber set to 29°C, z-interval 1µm. Laser settings were kept constant in all experiments. Images were acquired during macrophage invasion into the gb (St 12). Pseudo-coloring was conducted for the mCherry red channel. Each pixel in the image has a color ascribed to it via the fire "Look Up Table" translating the level of intensity of the mCherry channel into a defined amount of each color. The highest intensity of the image is represented as very bright yellow and all other grey values are depicted as colors on the scale accordingly.

For quantification of Moe::3xmCherry intensity, an ROI was drawn in Fiji software around macrophages at the germband entry site in 20 z-stacks for each embryo. The area mean intensity was measured in all ROIs and the average/embryo was calculated. To normalize fluorescence intensities per batch, the average intensity/embryo of all ROIs in each sample was divided by the arithmetic mean of the average intensity/embryo of all ROIs in the control per batch. The normalized average intensities/embryo were then compared to each other using a t-test with Welch's correction for *DfosDN* and one way-ANOVA for *cher RNAi* and *TM4SF RNAi*.

Cell aspect ratio analysis and imaging actin dynamics

Laterally oriented embryos were used to measure the maximal length and width of macrophages expressing *UAS-CLIP::GFP* under the control of *srpHemoGal4*. Briefly, 3D-stacks with 1 µm Z resolution were acquired every 35-45 seconds for approximately 1 hour. As the strength of the GAL4 expression increased over time, laser power was adjusted

bioRxiv preprint doi: https://doi.org/10.1101/2020.09.18.301481; this version posted September 18, 2020. The copyright holder for this preprint (which was not certified by peer review) is the author/funder, who has granted bioRxiv a license to display the preprint in perpetuity. It is made available under aCC-BY-NC-ND 4.0 International license.

during acquisition to reach the best possible quality of visualization. Images acquired from mutiphoton microscopy were initially processed with ImSpector software (LaVision Bio Tec) to compile channels from the imaging data.

We started measuring from the time the cell body of the first macrophage fully appeared at the interface between the ectoderm and mesoderm and yolk sac until it had moved 30 µm along the ectoderm mesoderm interface. At each timeframe, a line was drawn in Fiji along the longest dimension of the macrophage in the direction of its front-rear polarization axis, denoted the maximal cell length, and along the orthologonal longest dimension, which was considered maximal cell width. We did not observe long CLIP::GFP protrusions, but when a small protrusion was present, it was not included in the length measurement; within this gb region the front of the first macrophage was clearly outlined with CLIP::GFP. The border between the first and second entering macrophages was drawn based on the uninterrupted intense line of CLIP::GFP at the base of the first macrophage; only cells with a clearly visible border were measured. The length to width ratio was quantified for each timeframe and a probability density function was plotted: 5 embryos were recorded for each genotype.

Imaging the actin protrusion

Laterally oriented embryos expressing *srpHemo-Gal4 UAS-LifeAct::GFP* were used to image macrophage actin live with a 3D-stack resolution of 1μm. See above description of CLIP::GFP labeled macrophage imaging for laser power and image compilation. Laser power was also increased further in the DfosDN samples to enhance actin visualization. We measured the length of the filopodia-like protrusion of the first entering macrophage with Imaris software (Bitplane) from the time when the protrusion was inserted into the ectoderm, mesoderm and yolk sac interface until the macrophage started to translocate its cell body into that location.

bioRxiv preprint doi: https://doi.org/10.1101/2020.09.18.301481; this version posted September 18, 2020. The copyright holder for this preprint (which was not certified by peer review) is the author/funder, who has granted bioRxiv a license to display the preprint in perpetuity. It is made available under aCC-BY-NC-ND 4.0 International license.

831

832 **FACS sorting of macrophages**

833 Adult flies of either *w;+;srpHemoGal4,srpHemo::3xmCherry/+* or *w;+;*

834 *srpHemoGal4,srpHemo::3xmCherry /UASDfosDN* genotypes were placed into plastic cages

835 closed with apple juice plates with applied yeast to enhance egg laying. Collections were

836 performed at 29°C for 1 hour, then kept at 29°C for additional 5 hours 15 minutes to reach

837 stage 11-early stage 12. Embryos were harvested for 2 days with 6-7 collections per day and

838 stored meanwhile at +4°C to slow down development. Collected embryos were dissociated

839 and the macrophages sorted as previously described (Gyoergy et al., 2018). About 1-1.5x10^5

840 macrophages were sorted within 30 minutes.

841

842 **Sequencing of the macrophage transcriptome**

843 Total RNA was isolated from FACS-sorted macrophages using Qiagen RNeasy Mini kit (Cat

844 No. 74104). The quality and concentration of RNA was determined using Agilent 6000 Pico

845 kit (Cat No. 5067-1513) on an Agilent 2100 Bioanalyzer: on average about 100 ng of total

846 RNA was extracted from 1.5x10^5 macrophages. RNA sequencing was performed by the CSF

847 facility of Vienna Biocenter according to standard procedures

848 (https://www.vbcf.ac.at/facilities/next-generation-sequencing/) on three replicates. Briefly,

849 the cDNA library was synthesized using QuantSeq 3' mRNA-seq Library Prep kit and

850 sequenced on the Illumina HiSeq 2500 platform. The reads were mapped to the *Drosophila*

851 *melanogaster* Ensembl BDGP6 reference genome with STAR (version 2.5.1b) The read

852 counts for each gene were detected using HTSeq (version 0.5.4p3). The Flybase annotation

853 (r6.19) was used in both mapping and read counting. Counts were normalised to arbitrary

854 units using the TMM normalization from edgeR package in R. Prior to statistical testing the

855 data was voom transformed and then the differential expression between the sample groups

bioRxiv preprint doi: https://doi.org/10.1101/2020.09.18.301481; this version posted September 18, 2020. The copyright holder for this preprint (which was not certified by peer review) is the author/funder, who has granted bioRxiv a license to display the preprint in perpetuity. It is made available under aCC-BY-NC-ND 4.0 International license.

was calculated with limma package in R. The functional analyses were done using the topGO and gage packages in R (Anders, Pyl, & Huber, 2015; Dobin et al., 2013).

Primer	Sequence
Fos fw	ATGGTGAAGACCGTGTCAGG
Fos_rv	GTTGATCTGTCTCCGCTTGGA
Flna_fw	GTCACAGTGTCAATCGGAGGT
Flna_rv	TTGCCTGCTGCTTTTGTGTC
Flnb_fw	TTCTACACTGCTGCCAAGCC
Flnb_rv	CTGTAACCCAGGGCCTGAATC
Flnc_fw	CATCACCCGGAGTCCTTTCC
Flnc_rv	CTCTGTGCCCTTTGGACCTT
Tspan6_fw	TCGAACTAGTTGCCGCCATT
Tspan6_rv	CCGCAACAATGCAACGTACT
Gstt3_fw	GGAGCTCTACCTGGACCTGA
Gstt3_rv	AAGATGGCCACACTCTCTGC
Eva1c_fw	GTTGCCTACGCATGTGTTCC
Eva1c_rv	CCGATGCAGACACTGGACAT
Tspo_fw	GTATTCAGCCATGGGGTATGG
Tspo_rv	AAGCAGAAGATCGGCCAAGG
Tbp_fw	GGGGAGCTGTGATGTGAAGT
Tbp_rv	CCAGGAAATAATTCTGGCTCAT

qRT-PCR analysis of mRNA levels in murine bones and osteosarcomas

RNA isolation and qPCR was performed from bones of wild-type C57BL/6 mice and from bones and osteosarcomas (OS) of H2-c-fosLTR as previously described with the above primers (Rüther et al., 1989).

Statistical and Repeatability

Mouse experiments:

Data are shown as mean ± SEM. One-way ANOVA followed by Tukey's multiple comparisons post-test was applied to compare experimental groups. Statistical analysis was performed using GrapPad Prism 6.0 software. A p-value <0.05 was considered statistically significant (*p<0.05, **p<0.01, ***p<0.001, ****p<0.0001).

Drosophila experiments:

bioRxiv preprint doi: https://doi.org/10.1101/2020.09.18.301481; this version posted September 18, 2020. The copyright holder for this preprint (which was not certified by peer review) is the author/funder, who has granted bioRxiv a license to display the preprint in perpetuity. It is made available under aCC-BY-NC-ND 4.0 International license.

Statistical tests as well as the number of embryos/cells/tracks/contacts assessed are listed in the Figure legends. All statistical analyses were performed using GraphPad PRISM or R Studio and significance was determined using a 95% confidence interval. No statistical method was used to predetermine sample size. An unpaired t-test and Mann-Whitney U Test were used to calculate the significance in differences between two groups and One-Way ANOVA followed by Tukey HSD post hoc test was used for multiple comparisons.

Representative images of Dfos antibody staining were analyzed per replicate per genotype and *in situ* hybridization are from experiments that were repeated 2 times with many embryos with reproducible results. Representative images and plots of different *Dfos* mutants in Fig 1 and S1 Fig are from experiments that were repeated 2-3 times. In live imaging experiments in Fig 2 and S2 Fig, 3-7 embryos for each genotype were analyzed, each embryo was recorded in a separate day. Three replicates were conducted of FACS sorting macrophages from embryos, and then preparing RNA samples for RNA sequencing for each genotype. Representative images and plots of RNAi and rescue experiments in Fig 4 and S4 Fig are from experiments that were repeated 2-3 times. Representative images and plots of phalloidin immunostaining in Fig 4 are from experiments that were repeated 4 times. For all immunostaining experiments 3-7 embryos were analyzed per replicate per genotype. In Moe::3xmCherry experiments in Fig 4D, 11 and 12 embryos were analysed for the control and *DfosDN*, and in Fig 4E 10, 8, and 8 embryos were analysed for the control, *cher RNAi*, and *TM4SF RNAi* respectively, as indicated in the graph and in the relevant part of the F-actin reporter measurement section of the methods. In the LifeAct::GFP protrusion live imaging experiment in Fig 5 and S5 Fig, 3-5 embryos were analyzed for each genotype. In CLIP::GFP live imaging experiments in Fig 5 and S5 Fig, 5-6 embryos were analyzed for each genotype for the cell aspect ratio in germband zone, and 2 embryos in pre-germband zone and for tracking of the front vs rear speed. Each embryo was recorded on a separate

bioRxiv preprint doi: https://doi.org/10.1101/2020.09.18.301481; this version posted September 18, 2020. The copyright holder for this preprint (which was not certified by peer review) is the author/funder, who has granted bioRxiv a license to display the preprint in perpetuity. It is made available under aCC-BY-NC-ND 4.0 International license.

day. The Lamin over expression in S5 Fig and the Lamin knockdown rescue experiments in Fig 5G were repeated at least 3 times with reproducible results. Gb rescue experiment in Fig 5H was repeated at least 4 times with reproducible results.

Acknowledgements

We thank the following for their contributions: The *Drosophila* Genomics Resource Center supported by NIH grant 2P40OD010949-10A1 for plasmids, K. Brueckner. B. Stramer, M. Uhlirova, O. Schuldiner, the Bloomington *Drosophila* Stock Center supported by NIH grant P40OD018537 and the Vienna *Drosophila* Resource Center for fly stocks, FlyBase (Thurmond et al., 2019) for essential genomic information, and the BDGP *in situ* database for data (Tomancak et al., 2002, 2007). For antibodies, we thank the Developmental Studies Hybridoma Bank, which was created by the Eunice Kennedy Shriver National Institute of Child Health and Human Development of the NIH, and is maintained at the University of Iowa, as well as J. Zeitlinger for her generous gift of Dfos antibody. We thank the Vienna BioCenter Core Facilities for RNA sequencing and analysis and the Life Scientific Service Units at IST Austria for technical support and assistance with microscopy and FACS analysis. We thank C.P. Heisenberg, P. Martin, M. Sixt and Siekhaus group members for discussions and T.Hurd, A. Ratheesh and P. Rangan for comments on the manuscript. A.G. was supported by the Austrian Science Fund (FWF) grant DASI_FWF01_P29638S, D.E.S. by Marie Curie CIG 334077/IRTIM. M.S. is supported by the FWF, PhD program W1212 and the European Research Council (ERC) Advanced grant (ERC-2015-AdG TNT-Tumors 694883). S.W. is supported by an OEAW, DOC fellowship.

bioRxiv preprint doi: https://doi.org/10.1101/2020.09.18.301481; this version posted September 18, 2020. The copyright holder for this preprint (which was not certified by peer review) is the author/funder, who has granted bioRxiv a license to display the preprint in perpetuity. It is made available under aCC-BY-NC-ND 4.0 International license.

References

Anders, S., Pyl, P. T., & Huber, W. (2015). HTSeq-A Python framework to work with high-throughput sequencing data. *Bioinformatics*, *31*(2), 166–169. https://doi.org/10.1093/bioinformatics/btu638

Andrés, V., & González, J. M. (2009). Role of A-type lamins in signaling, transcription, and chromatin organization. *Journal of Cell Biology*, *187*(7), 945–957. https://doi.org/10.1083/jcb.200904124

Bellanger, J. M., Astier, C., Sardet, C., Ohta, Y., Stossel, T. P., & Debant, A. (2000). The Rac1- and RhoG-specific GEF domain of trio targets filamin to remodel cytoskeletal actin. *Nature Cell Biology*, *2*(12), 888–892. https://doi.org/10.1038/35046533

Benhra, N., Barrio, L., Muzzopappa, M., & Milán, M. (2018). Chromosomal Instability Induces Cellular Invasion in Epithelial Tissues. *Developmental Cell*, *47*(2), 161-174.e4. https://doi.org/10.1016/j.devcel.2018.08.021

Berditchevski, F., & Odintsova, E. (1999). Characterization of integrin-tetraspanin adhesion complexes: Role of tetraspanins in integrin signaling. *Journal of Cell Biology*, *146*(2), 477–492. https://doi.org/10.1083/jcb.146.2.477

Bershadsky, A. D., Balaban, N. Q., & Geiger, B. (2003). Adhesion-Dependent Cell Mechanosensitivity. *Annual Review of Cell and Developmental Biology*, *19*(1), 677–695. https://doi.org/10.1146/annurev.cellbio.19.111301.153011

Bilancia, C. G., Winkelman, J. D., Tsygankov, D., Nowotarski, S. H., Sees, J. A., Comber, K., … Peifer, M. (2014). Enabled negatively regulates diaphanous-driven actin dynamics in vitro and in vivo. *Developmental Cell*, *28*(4), 394–408. https://doi.org/10.1016/j.devcel.2014.01.015

Bosch, P.S., Makhijani, K., Herboso, L., Gold, K.S., Baginsky, R., Woodcock, K.J., Alexander, B., Kukar, K., Corcoran, S., Jacobs, T., Ouyang, D., Wong, C., Ramond, E.J.V., Rhiner, C., Moreno, E., Lemaitre, B., Geissmann, F., & Brueckner, K. (2019). Adult *Drosophila* lack hematopoiesis but rely on a blood cell reservoir at the respiratory epithelia to relay infection signals to surrounding tissues. *Developmental Cell*, *51*(6)787-803. https://doi.org/10.1016/j.devcel.2019.10.017

Brock, A. R., Wang, Y., Berger, S., Renkawitz-Pohl, R., Han, V. C., Wu, Y., & Galko, M. J. (2012). Transcriptional regulation of profilin during wound closure in Drosophila larvae. *Journal of Cell Science*, *125*(23), 5667–5676. https://doi.org/10.1242/jcs.107490

Brückner, K., Kockel, L., Duchek, P., Luque, C. M., Rørth, P., & Perrimon, N. (2004). The PDGF/VEGF

bioRxiv preprint doi: https://doi.org/10.1101/2020.09.18.301481; this version posted September 18, 2020. The copyright holder for this preprint (which was not certified by peer review) is the author/funder, who has granted bioRxiv a license to display the preprint in perpetuity. It is made available under aCC-BY-NC-ND 4.0 International license.

947 receptor controls blood cell survival in Drosophila. *Developmental Cell*, *7*(1), 73–84.
948 https://doi.org/10.1016/j.devcel.2004.06.007
949 Brzozowski, J. S., Bond, D. R., Jankowski, H., Goldie, B. J., Burchell, R., Naudin, C., … Weidenhofer, J.
950 (2018). Extracellular vesicles with altered tetraspanin CD9 and CD151 levels confer increased prostate
951 cell motility and invasion. *Scientific Reports*, *8*(1). https://doi.org/10.1038/s41598-018-27180-z
952 Butcher, D.T., Alliston, T. & Weaver, V.M.(2009). A tense situation: forcing tumour progression. *Nature*
953 *Reviews Cancer, 9*(2), 108-22. . https://doi.org/10.11038/nrc2544
954 Cho, N. K., Keyes, L., Johnson, E., Heller, J., Ryner, L., Karim, F., & Krasnow, M. A. (2002). Developmental
955 control of blood cell migration by the Drosophila VEGF pathway. *Cell*, *108*(6).
956 https://doi.org/10.1016/S0092-8674(02)00676-1
957 Chugh, P., Clark, A. G., Smith, M. B., Cassani, D. A. D., Dierkes, K., Ragab, A., … Paluch, E. K. (2017). Actin
958 cortex architecture regulates cell surface tension. *Nature Cell Biology*, *19*(6), 689–697.
959 https://doi.org/10.1038/ncb3525
960 Danuser, G., Allard, J., & Mogilner, A. (2013). Mathematical Modeling of Eukaryotic Cell Migration: Insights
961 Beyond Experiments. *Annual Review of Cell and Developmental Biology*, *29*(1).
962 https://doi.org/10.1146/annurev-cellbio-101512-122308
963 Davidson, A. J., Millard, T. H., Evans, I. R., & Wood, W. (2019). Ena orchestrates remodelling within the actin
964 cytoskeleton to drive robust Drosophila macrophage chemotaxis. *Journal of Cell Science*, *132*(5).
965 https://doi.org/10.1242/jcs.224618
966 Davidson, P.M., Denais, C., Bakshi, M., & Lammerding, J. (2014).. Nuclear deformability constitutes a rate-
967 limiting step during cell migration in 3-D environments. *Cellular and Molecular Bioengineering,*
968 *7*(3)293-306. https://doi.org/10.1007/s12195-014-0342-y
969 Davis, J. R., Luchici, A., Miodownik, M., Stramer, B. M., Davis, J. R., Luchici, A., … Stramer, B. M. (2015).
970 Inter-Cellular Forces Orchestrate Contact Inhibition of Locomotion Article Inter-Cellular Forces
971 Orchestrate Contact Inhibition of Locomotion. *Cell*, *161*(2), 361–373.
972 https://doi.org/10.1016/j.cell.2015.02.015
973 Delaguillaumie, A., Lagaudrière-Gesbert, C., Popoff, M. R., & Conjeaud H., H. (2002). Rho GTPase link
974 cytoskeletal rearrangements and activation processes induced via the tetraspanin CD82 in T lymphocytes.
975 *Journal of Cell Science*, *115*(2).
976 Deluca, T. F., Cui, J., Jung, J. Y., St. Gabriel, K. C., & Wall, D. P. (2012). Roundup 2.0: Enabling comparative

bioRxiv preprint doi: https://doi.org/10.1101/2020.09.18.301481; this version posted September 18, 2020. The copyright holder for this preprint (which was not certified by peer review) is the author/funder, who has granted bioRxiv a license to display the preprint in perpetuity. It is made available under aCC-BY-NC-ND 4.0 International license.

977 genomics for over 1800 genomes. *Bioinformatics*, *28*(5). https://doi.org/10.1093/bioinformatics/bts006

978 Dobin, A., Davis, C. A., Schlesinger, F., Drenkow, J., Zaleski, C., Jha, S., … Gingeras, T. R. (2013). STAR:
979 Ultrafast universal RNA-seq aligner. *Bioinformatics*, *29*(1), 15–21.
980 https://doi.org/10.1093/bioinformatics/bts635

981 Duffy, J. B. (2002). GAL4 system in Drosophila: A fly geneticist's Swiss army knife. *Genesis*, *34*(1–2), 1–15.
982 https://doi.org/10.1002/gene.10150

983 Edwards, K. A., Demsky, M., Montague, R. A., Weymouth, N., & Kiehart, D. P. (1997). GFP-moesin
984 illuminates actin cytoskeleton dynamics in living tissue and demonstrates cell shape changes during
985 morphogenesis in Drosophila. *Developmental Biology*, *191*(1). https://doi.org/10.1006/dbio.1997.8707

986 Ehrlicher, A. J., Nakamura, F., Hartwig, J. H., Weitz, D. A., & Stossel, T. P. (2011). Mechanical strain in actin
987 networks regulates FilGAP and integrin binding to filamin A. *Nature*, *478*(7368), 260–263.
988 https://doi.org/10.1038/nature10430

989 Eresh, S., Riese, J., Jackson, D. B., Bohmann, D., & Bienz, M. (1997). A CREB-binding site as a target for
990 decapentaplegic signalling during Drosophila endoderm induction. *EMBO Journal*, *16*(8), 2014–2022.
991 https://doi.org/10.1093/emboj/16.8.2014

992 Evans, I. R., & Wood, W. (2011). Drosophila embryonic hemocytes. *Current Biology*, *21*(5), R173–R174.
993 https://doi.org/10.1016/j.cub.2011.01.061

994 Franck, Z., Gary, R., & Bretscher, A. (1993). Moesin, like ezrin, colocalizes with actin in the cortical
995 cytoskeleton in cultured cells, but its expression is more variable. *Journal of Cell Science*, *105*(1).

996 Fujita, M., Mitsuhashi, H., Isogai, S., Nakata, T., Kawakami, A., Nonaka, I., … Kudo, A. (2012). Filamin C
997 plays an essential role in the maintenance of the structural integrity of cardiac and skeletal muscles,
998 revealed by the medaka mutant zacro. *Developmental Biology*, *361*(1), 79–89.
999 https://doi.org/10.1016/j.ydbio.2011.10.008

1000 García-Echeverría, C. Methionine-containing zipper peptides. *Lett Pept Sci* **4,** 135–140 (1997).
1001 https://doi.org/10.1007/BF02443525

1002 Ginhoux, F.& Guilliams, M. (2016). Tissue-resident macrophage ontogeny and homeostasis. *Immunity 44*(3),
1003 439-449. https://doi.org/10.1016/j.immuni.2016.02.024

1004 Glogauer, M., Arora, P., Chou, D., Janmey, P. A., Downey, G. P., & McCulloch, C. A. G. (1998). The role of
1005 actin-binding protein 280 in integrin-dependent mechanoprotection. *Journal of Biological Chemistry*,
1006 *273*(3), 1689–1698. https://doi.org/10.1074/jbc.273.3.1689

bioRxiv preprint doi: https://doi.org/10.1101/2020.09.18.301481; this version posted September 18, 2020. The copyright holder for this preprint (which was not certified by peer review) is the author/funder, who has granted bioRxiv a license to display the preprint in perpetuity. It is made available under aCC-BY-NC-ND 4.0 International license.

1007 Glover, J.N.M. and Harrison, S.C. (1005). Crystal structure of the heterodimeric bZIP transcritpion factor c-Fos-
1008 c-Jun bound to DNA. *Nature, 373*(6511):257-261. https://doi.org/10.1038/373257a0
1009 Goldmann, W. H., Tempel, M., Sprenger, I., Isenberg, G., & Ezzell, R. M. (1997). Viscoelasticity of actin-
1010 gelsolin networks in the presence of filamin. *European Journal of Biochemistry*, *246*(2), 373–379.
1011 https://doi.org/10.1111/j.1432-1033.1997.00373.x
1012 Gonzalez-Gaitan, M. & Peifer, M. (2009) Exploring the roles of Diaphanous and Enabled activity in shaping the
1013 balance between filopodia and lamellipodia. *Molecular Biology of the Cell 20*(24).
1014 https://doi.org/10.1091/mbc.e09-02-0144
1015 Greten, F.R. & Grovennikov, S.I. (2019). Inflammation and Cancer: Triggers, Mechanisms and Consequences.
1016 *Immunity 51*(1), 27-41. https://doi.org/10.1016/j.immuni.2019.06.025
1017 Großhans, J., Wenzl, C., Herz, H. M., Bartoszewski, S., Schnorrer, F., Vogt, N., … Müller, H. A. (2005).
1018 RhoGEF2 and the formin Dia control the formation of the furrow canal by directed actin assembly during
1019 Drosophila cellularisation. *Development*, *132*(5), 1009–1020. https://doi.org/10.1242/dev.01669
1020 Guilliams, M., Thierry, G.R., Bonnardel, J., & Bajenoff, M. (2020). Establishment and Maintenance of the
1021 Macrophage Niche. *Immunity 52*(3), 434-451. https://doi.org/10.1016/j.immuni.2020.02.015
1022 Gyoergy, A., Roblek, M., Ratheesh, A., Valoskova, K., Belyaeva, V., Wachner, S., … Siekhaus, D. E. (2018).
1023 Tools allowing independent visualization and genetic manipulation of Drosophila melanogaster
1024 macrophages and surrounding tissues. *G3: Genes, Genomes, Genetics*, *8*(3).
1025 https://doi.org/10.1534/g3.117.300452
1026 Hammonds, A. A. S., Bristow, C. C. a, Fisher, W. W., Weiszmann, R., Wu, S., Hartenstein, V., … Celniker, S.
1027 E. (2013). Spatial expression of transcription factors in Drosophila embryonic organ development.
1028 *Genome Biology*, *14*(12), R140. https://doi.org/10.1186/gb-2013-14-12-r140
1029 Harada, T., Swift, J., Irianto, J., Shin, J, Spinler, K.R., Athirasala, A., Diegmiller, R., Dingal, P.C.D.P.,
1030 Ivanovska, I.L., & Discher, D.E. (2014). Nuclear lamin stiffness is a barrier to 3D migration, but softness
1031 can limit survival. J. Cell Biology, 2014(5)669-82. https://doi.org/10.1083/jcb.201308029.
1032 Heer, N. C., & Martin, A. C. (2017). Tension, contraction and tissue morphogenesis. *Development (Cambridge)*,
1033 *144*(23). https://doi.org/10.1242/dev.151282
1034 Holz, A., Bossinger, B., Strasser, T., Janning, W., & Klapper, R. (2003). The two origins of hemocytes in
1035 *Drosophila. Development, 130*(20), 4955-62. https://doi.org/10.1242/dev.007202
1036 Hong, I. K., Jeoung, D. Il, Ha, K. S., Kim, Y. M., & Lee, H. (2012). Tetraspanin CD151 stimulates adhesion-

bioRxiv preprint doi: https://doi.org/10.1101/2020.09.18.301481; this version posted September 18, 2020. The copyright holder for this preprint (which was not certified by peer review) is the author/funder, who has granted bioRxiv a license to display the preprint in perpetuity. It is made available under aCC-BY-NC-ND 4.0 International license.

dependent activation of Ras, Rac, and Cdc42 by facilitating molecular association between β1 integrins and small GTPases. *Journal of Biological Chemistry*, *287*(38), 32027–32039. https://doi.org/10.1074/jbc.M111.314443

Hu, J., Lu, J., Lian, G., Ferland, R. J., Dettenhofer, M., & Sheen, V. L. (2014). Formin 1 and filamin B physically interact to coordinate chondrocyte proliferation and differentiation in the growth plate. *Human Molecular Genetics*, *23*(17), 4663–4673. https://doi.org/10.1093/hmg/ddu186

Kasza, K. E., Broedersz, C. P., Koenderink, G. H., Lin, Y. C., Messner, W., Millman, E. A., … Weitz, D. A. (2010). Actin filament length tunes elasticity of flexibly cross-linked actin networks. *Biophysical Journal*, *99*(4), 1091–1100. https://doi.org/10.1016/j.bpj.2010.06.025

Kessenbrock, K., Plaks, V., & Werb, Z. (2010). Matrix metalloproteinases: regulators of the tumor microenvironment. *Cell 141*(1), 52-67. https://doi.org/10.1016/j.cell.2010.03.015

Kühn, S., & Geyer, M. (2014). Formins as effector proteins of rho GTPases. *Small GTPases*, *5*(JUNE). https://doi.org/10.4161/sgtp.29513

Külshammer, E., Mundorf, J., Kilinc, M., Frommolt, P., Wagle, P., & Uhlirova, M. (2015). Interplay among Drosophila transcription factors Ets21c, Fos and Ftz-F1 drives JNK-mediated tumor malignancy. *DMM Disease Models and Mechanisms*, *8*(10), 1279–1293. https://doi.org/10.1242/dmm.020719

Külshammer, E., & Uhlirova, M. (2013). The actin cross-linker Filamin/Cheerio mediates tumor malignancy downstream of JNK signaling. *Journal of Cell Science*, *126*(4), 927–938. https://doi.org/10.1242/jcs.114462

Kumar, A., Shutova, M. S., Tanaka, K., Iwamoto, D. V., Calderwood, D. A., Svitkina, T. M., & Schwartz, M. A. (2019). Filamin A mediates isotropic distribution of applied force across the actin network. *Journal of Cell Biology*, *218*(8), 2481–2491. https://doi.org/10.1083/jcb.201901086

Lehmann, R., & Tautz, D. (1994). In Situ Hybridization to RNA. *Methods in Cell Biology*, *44*(C), 575–596. https://doi.org/10.1016/S0091-679X(08)60933-4

Lemaitre, B., & Hoffmann, J. (2007). The Host Defense of *Drosophila melanogaster*. *Annual Review of Immunology*, *25*(1), 697–743. https://doi.org/10.1146/annurev.immunol.25.022106.141615

Lesch, C., Jo, J., Wu, Y., Fish, G. S., & Galko, M. J. (2010). A Targeted *UAS-RNAi* Screen in Drosophila Larvae Identifies Wound Closure Genes Regulating Distinct Cellular Processes. *Genetics*, *186*(3), 943–957. https://doi.org/10.1534/genetics.110.121822

Lian, G., Dettenhofer, M., Lu, J., Downing, M., Chenn, A., Wong, T., & Sheen, V. (2016). Filamin A- and

bioRxiv preprint doi: https://doi.org/10.1101/2020.09.18.301481; this version posted September 18, 2020. The copyright holder for this preprint (which was not certified by peer review) is the author/funder, who has granted bioRxiv a license to display the preprint in perpetuity. It is made available under aCC-BY-NC-ND 4.0 International license.

formin 2-dependent endocytosis regulates proliferation via the canonical wnt pathway. *Development (Cambridge)*, *143*(23). https://doi.org/10.1242/dev.139295

Linder, M., Glitzner, E., Srivatsa, S., Bakiri, L., Matsuoka, K., Shahrouzi, P., … Sibilia, M. (2018). EGFR is required for FOS□dependent bone tumor development via RSK2/CREB signaling. *EMBO Molecular Medicine*, *10*(11). https://doi.org/10.15252/emmm.201809408

Luster, A. D., Alon, R., & von Andrian, U. H. (2005). Immune cell migration in inflammation: Present and future therapeutic targets. *Nature Immunology*, *6*(12), 1182–1190. https://doi.org/10.1038/ni1275

Makhijani, K., Alexander, B., Tanaka, T., Rulfson, E., & Brückner, K. (2011). The peripheral nervous system supports blood cell homing and survival in the Drosophila larva. *Development, 138*(24), 5379-91. https://doi.org/10.1242/dev.067322

Matsubayashi, Y., Louani, A., Dragu, A., Sánchez-Sánchez, B. J., Serna-Morales, E., Yolland, L., … Stramer, B. M. (2017). A Moving Source of Matrix Components Is Essential for De Novo Basement Membrane Formation. *Current Biology*, *27*(22), 3526-3534.e4. https://doi.org/10.1016/j.cub.2017.10.001

Min, P. I., Spurney, R. F., Qisheng, T. U., Hinson, T., & Darryl Quarles, L. (2002). Calcium-sensing receptor activation of Rho involves filamin and rho-guanine nucleotide exchange factor. *Endocrinology*, *143*(10), 3830–3838. https://doi.org/10.1210/en.2002-220240

Mitchison, T.J., and Cramer, L.P. (1996) Actin-based cell motility and cell locomotion. *Cell 84*(3)371-9). https://doi.org/10.1016/s0092-8864(00)81281-7.

Muñoz-Alarcón, A., Pavlovic, M., Wismar, J., Schmitt, B., Eriksson, M., Kylsten, P., & Dushay, M. S. (2007). Characterization of lamin mutation phenotypes in Drosophila and comparison to human laminopathies. *PloS One*, *2*(6). https://doi.org/10.1371/journal.pone.0000532

Ohta, Y., Suzuki, N., Nakamura, S., Hartwig, J. H., & Stossel, T. P. (1999). The small GTPase RaIA targets filamin to induce filopodia. *Proceedings of the National Academy of Sciences of the United States of America*, *96*(5), 2122–2128. https://doi.org/10.1073/pnas.96.5.2122

Paluch, E. K., Aspalter, I. M., & Sixt, M. (2016). Focal Adhesion–Independent Cell Migration. *Annual Review of Cell and Developmental Biology*, *32*(1), 469–490. https://doi.org/10.1146/annurev-cellbio-111315-125341

Perez-Hernandez, D., Gutiérrez-Vázquez, C., Jorge, I., López-Martín, S., Ursa, A., Sánchez-Madrid, F., … Yañez-Mó, M. (2013). The intracellular interactome of tetraspanin-enriched microdomains reveals their function as sorting machineries toward exosomes. *Journal of Biological Chemistry*, *288*(17), 11649–

bioRxiv preprint doi: https://doi.org/10.1101/2020.09.18.301481; this version posted September 18, 2020. The copyright holder for this preprint (which was not certified by peer review) is the author/funder, who has granted bioRxiv a license to display the preprint in perpetuity. It is made available under aCC-BY-NC-ND 4.0 International license.

11661. https://doi.org/10.1074/jbc.M112.445304

Perkins, L. A., Holderbaum, L., Tao, R., Hu, Y., Sopko, R., McCall, K., … Perrimon, N. (2015). The transgenic RNAi project at Harvard medical school: Resources and validation. *Genetics*, *201*(3), 843–852. https://doi.org/10.1534/genetics.115.180208

Popowicz, G. M., Schleicher, M., Noegel, A. A., & Holak, T. A. (2006). Filamins: promiscuous organizers of the cytoskeleton. *Trends in Biochemical Sciences*, *31*(7), 411–419. https://doi.org/10.1016/j.tibs.2006.05.006

Raab, M., Gentili, M., de Belly, H., Thiam, H.R., Vargas, P., Jimenez, A.J., Lautenschlaeger, F., Voituriez, R., Lennon-Duménil, A.M., Manel, N, Piel, M. (2016). ESCRT III repairs nuclear envelope ruptures during cell migration to limit DNA damage and cell death. Science, 352(6283), 359-62. https://doi.org/10.1126/science.aad7611

Ratheesh, A., Belyaeva, V., & Siekhaus, D. E. (2015). Drosophila immune cell migration and adhesion during embryonic development and larval immune responses. *Current Opinion in Cell Biology*, *36*, 71–79. https://doi.org/10.1016/j.ceb.2015.07.003

Ratheesh, A., Biebl, J., Vesela, J., Smutny, M., Papusheva, E., Krens, S. F. G., … Siekhaus, D. E. (2018). Drosophila TNF Modulates Tissue Tension in the Embryo to Facilitate Macrophage Invasive Migration. *Developmental Cell*, *45*(3), 331-346.e7. https://doi.org/10.1016/j.devcel.2018.04.002

Razinia, Z., Mäkelä, T., Ylänne, J., & Calderwood, D. A. (2012). Filamins in Mechanosensing and Signaling. *Annual Review of Biophysics*, *41*(1), 227–246. https://doi.org/10.1146/annurev-biophys-050511-102252

Riesgo-Escovar, J. R., & Hafen, E. (1997). Common and distinct roles of DFos and DJun during Drosophila development. *Science (New York, N.Y.)*, *278*(5338), 669–672. https://doi.org/10.1126/science.278.5338.669

Riveline, D., Zamir, E., Balaban, N. Q., Schwarz, U. S., Ishizaki, T., Narumiya, S., … Bershadsky, A. D. (2001). Focal contacts as mechanosensors: Externally applied local mechanical force induces growth of focal contacts by an mDia1-dependent and ROCK-independent mechanism. *Journal of Cell Biology*, *153*(6), 1175–1185. https://doi.org/10.1083/jcb.153.6.1175

Rose, R., Weyand, M., Lammers, M., Ishizaki, T., Ahmadian, M. R., & Wittinghofer, A. (2005). Structural and mechanistic insights into the interaction between Rho and mammalian Dia. *Nature*, *435*(7041), 513–518. https://doi.org/10.1038/nature03604

Rousso, T., Shewan, A. M., Mostov, K. E., Schejter, E. D., & Shilo, B. Z. (2013). Apical targeting of the formin

bioRxiv preprint doi: https://doi.org/10.1101/2020.09.18.301481; this version posted September 18, 2020. The copyright holder for this preprint (which was not certified by peer review) is the author/funder, who has granted bioRxiv a license to display the preprint in perpetuity. It is made available under aCC-BY-NC-ND 4.0 International license.

diaphanous in Drosophila tubular epithelia. *ELife*, *2013*(2). https://doi.org/10.7554/eLife.00666

Sánchez-Sánchez, B. J., Urbano, J. M., Comber, K., Dragu, A., Wood, W., Stramer, B., & Martín-Bermudo, M. D. (2017). Drosophila Embryonic Hemocytes Produce Laminins to Strengthen Migratory Response. *Cell Reports*, *21*(6), 1461–1470. https://doi.org/10.1016/j.celrep.2017.10.047

Seth, A., Otomo, C., & Rosen, M. K. (2006). Autoinhibition regulates cellular localization and actin assembly activity of the diaphanous-related formins FRLα and mDia1. *Journal of Cell Biology*, *174*(5), 701–713. https://doi.org/10.1083/jcb.200605006

Sharma, P. & Allison, J.P. (2015) The future of immune checkpoint therapy. *Science 348*(6230), 56-61. https://doi.org/10.1126/science.aaa8172.

Shigeta, M., Sanzen, N., Ozawa, M., Gu, J., Hasegawa, H., & Sekiguchi, K. (2003). CD151 regulates epithelial cell-cell adhesion through PKC- and Cdc42-dependent actin cytoskeletal reorganization. *Journal of Cell Biology*, *163*(1), 165–176. https://doi.org/10.1083/jcb.200301075

Siekhaus, D., Haesemeyer, M., Moffitt, O., & Lehmann, R. (2010). RhoL controls invasion and Rap1 localization during immune cell transmigration in Drosophila. *Nature Cell Biology*, *12*(6), 605–610. https://doi.org/10.1038/ncb2063

Sit, S. T., & Manser, E. (2011). Rho GTPases and their role in organizing the actin cytoskeleton. *Journal of Cell Science*, *124*(5), 679–683. https://doi.org/10.1242/jcs.064964

Smutny, M., Ákos, Z., Grigolon, S., Shamipour, S., Ruprecht, V., Čapek, D., … Heisenberg, C. P. (2017). Friction forces position the neural anlage. *Nature Cell Biology*, *19*(4), 306–317. https://doi.org/10.1038/ncb3492

Sokol, N. S., & Cooley, L. (2003). Drosophila filamin is required for follicle cell motility during oogenesis. *Developmental Biology*, *260*(1), 260–272. https://doi.org/10.1016/S0012-1606(03)00248-3

Somogyi, K., & Rørth, P. (2004). Evidence for tension-based regulation of Drosophila MAL and SRF during invasive cell migration. *Developmental Cell*, *7*(1), 85–93. https://doi.org/10.1016/j.devcel.2004.05.020

Stossel, T. P., Condeelis, J., Cooley, L., Hartwig, J. H., Noegel, A., Schleicher, M., & Shapiro, S. S. (2001). Filamins as integrators of cell mechanics and signalling. *Nature Reviews Molecular Cell Biology*, *2*(2), 138–145. https://doi.org/10.1038/35052082

Szabo, P.A., Miron, M., & Farber, D.L. (2019). Location, location, location: Tissue residence memory T cells in mice and humans. *Science Immunology 4*(34), https://doi.org/10.1126/scieimunol.aas9673

Szalóki, N., Krieger, J. W., Komáromi, I., Tóth, K., & Vámosi, G. (2015). Evidence for Homodimerization of

bioRxiv preprint doi: https://doi.org/10.1101/2020.09.18.301481; this version posted September 18, 2020. The copyright holder for this preprint (which was not certified by peer review) is the author/funder, who has granted bioRxiv a license to display the preprint in perpetuity. It is made available under aCC-BY-NC-ND 4.0 International license.

the c-Fos Transcription Factor in Live Cells Revealed by Fluorescence Microscopy and Computer Modeling. *Molecular and Cellular Biology*, *35*(21). https://doi.org/10.1128/mcb.00346-15

Tejera, E., Rocha-Perugini, V., López-Martín, S., Prez-Hernández, D., Bachir, A. I., Horwitz, A. R., … Yáñez-Mo, M. (2013). CD81 regulates cell migration through its association with Rac GTPase. *Molecular Biology of the Cell*, *24*(3), 261–273. https://doi.org/10.1091/mbc.E12-09-0642

Termini, C. M., & Gillette, J. M. (2017). Tetraspanins Function as Regulators of Cellular Signaling. *Frontiers in Cell and Developmental Biology*, *5*, 34. https://doi.org/10.3389/fcell.2017.00034

Theret, M., Mounier, R., & Rossi, F. (2019). The origins and non-canonical functions of macrophages in development and regeneration. *Development, 146*(9). https://doi.org/10.1242/dev.156000

Thiam, H., Vargas, P., Carpi, N., Crespo, C.L., Raab, M., Terriac, E., King, M.C., Jacobelli, J., Alberts, A.S., Stradal, T., Lennon-Dumenil, A., Piel, M. (2016). Perinuclear Arp2/3-driven actin polymerization enables nuclear deformation to facilitate cell migration through complex environments. Stremmel:10997, https://doi.org/10.1038/ncomms10997

Thurmond, J., Goodman, J. L., Strelets, V. B., Attrill, H., Gramates, L. S., Marygold, S. J., … Baker, P. (2019). FlyBase 2.0: The next generation. *Nucleic Acids Research*, *47*(D1). https://doi.org/10.1093/nar/gky1003

Tomancak, P., Beaton, A., Weiszmann, R., Kwan, E., Shu, S. Q., Lewis, S. E., … Rubin, G. M. (2002). Systematic determination of patterns of gene expression during Drosophila embryogenesis. *Genome Biology*, *3*(12). https://doi.org/10.1186/gb-2002-3-12-research0088

Tomancak, P., Berman, B. P., Beaton, A., Weiszmann, R., Kwan, E., Hartenstein, V., … Rubin, G. M. (2007). Global analysis of patterns of gene expression during Drosophila embryogenesis. *Genome Biology*, *8*(7). https://doi.org/10.1186/gb-2007-8-7-r145

Tseng, Y., An, K. M., Esue, O., & Wirtz, D. (2004). The Bimodal Role of Filamin in Controlling the Architecture and Mechanics of F-actin Networks. *Journal of Biological Chemistry*, *279*(3), 1819–1826. https://doi.org/10.1074/jbc.M306090200

Uhlirova, M., & Bohmann, D. (2006). JNK- and Fos-regulated Mmp1 expression cooperates with Ras to induce invasive tumors in Drosophila. *EMBO Journal*, *25*(22), 5294–5304. https://doi.org/10.1038/sj.emboj.7601401

Vadlamudi, R. K., Li, F., Adam, L., Nguyen, D., Ohta, Y., Stossel, T. P., & Kumar, R. (2002). Filamin is essential in actin cytoskeletal assembly mediated by p21-activated kinase 1. *Nature Cell Biology*, *4*(9), 681–690. https://doi.org/10.1038/ncb838

bioRxiv preprint doi: https://doi.org/10.1101/2020.09.18.301481; this version posted September 18, 2020. The copyright holder for this preprint (which was not certified by peer review) is the author/funder, who has granted bioRxiv a license to display the preprint in perpetuity. It is made available under aCC-BY-NC-ND 4.0 International license.

Valoskova, K., Biebl, J., Roblek, M., Emtenani, S., Gyoergy, A., Misova, M., … Siekhaus, D. E. (2019). A conserved major facilitator superfamily member orchestrates a subset of O-glycosylation to aid macrophage tissue invasion. *ELife*, *8*. https://doi.org/10.7554/eLife.41801

Vetter, I.R., & Wittinghofer, A. (2001). The guanine nucleotide-binding switch in three dimensions. *Science 294(*5545),1299-1304. https://doi.org/10.1126/science.1062023

Warner, S. J., & Longmore, G. D. (2009). Cdc42 antagonizes Rho1 activity at adherens junctions to limit epithelial cell apical tension. *Journal of Cell Biology*, *187*(1), 119–133. https://doi.org/10.1083/jcb.200906047

Weavers, H., Evans, I. R., Martin, P., & Wood, W. (2016). Corpse Engulfment Generates a Molecular Memory that Primes the Macrophage Inflammatory Response. *Cell*. https://doi.org/10.1016/j.cell.2016.04.049

Williams, M. J., Habayeb, M. S., & Hultmark, D. (2007). Reciprocal regulation of Rac1 and Rho1 in Drosophila circulating immune surveillance cells. *Journal of Cell Science*, *120*(3), 502–511. https://doi.org/10.1242/jcs.03341

Wintner, O., Hirsch-Attas, N., Schlossberg, M., Brofman, F., Friedman, R., Kupervaser, M., … Buxboim, A. (2020). A Unified Linear Viscoelastic Model of the Cell Nucleus Defines the Mechanical Contributions of Lamins and Chromatin. *Advanced Science*, *7*(8). https://doi.org/10.1002/advs.201901222

Wood, W., Faria, C., & Jacinto, A. (2006). Distinct mechanisms regulate hemocyte chemotaxis during development and wound healing in Drosophila melanogaster. *Journal of Cell Biology*, *173*(3). https://doi.org/10.1083/jcb.200508161

Yáñez-Mó, M., Barreiro, O., Gordon-Alonso, M., Sala-Valdés, M., & Sánchez-Madrid, F. (2009). Tetraspanin-enriched microdomains: a functional unit in cell plasma membranes. *Trends in Cell Biology*, *19*(9), 434–446. https://doi.org/10.1016/j.tcb.2009.06.004

Yeung, L., Hickey, M.J., & Wright, M.D. (2018) The many and varied roles of tetraspanins in immune cell recrutment and migration. Frontiers in Immunology.9:1644 .https:// doi: 10.3389/fimmu.2018.01644.

Zeitlinger, J., Kockel, L., Peverali, F. A., Jackson, D. B., Mlodzik, M., & Bohmann, D. (1997). Defective dorsal closure and loss of epidermal decapentaplegic expression in Drosophila fos mutants. *EMBO Journal*, *16*(24), 7393–7401. https://doi.org/10.1093/emboj/16.24.7393

Zhang, X. A., Bontrager, A. L., & Hemler, M. E. (2001). Transmembrane-4 Superfamily Proteins Associate with Activated Protein Kinase C (PKC) and Link PKC to Specific β1 Integrins. *Journal of Biological Chemistry*, *276*(27), 25005–25013. https://doi.org/10.1074/jbc.M102156200

bioRxiv preprint doi: https://doi.org/10.1101/2020.09.18.301481; this version posted September 18, 2020. The copyright holder for this preprint (which was not certified by peer review) is the author/funder, who has granted bioRxiv a license to display the preprint in perpetuity. It is made available under aCC-BY-NC-ND 4.0 International license.

1217 Zhou, J., Kim, H. Y., & Davidson, L. A. (2009). Actomyosin stiffens the vertebrate embryo during crucial
1218 stages of elongation and neural tube closure. *Development*, *136*(4), 677–688.
1219 https://doi.org/10.1242/dev.026211
1220 Zimmerman, B., Kelly, B., McMillan, B. J., Seegar, T. C. M., Dror, R. O., Kruse, A. C., & Blacklow, S. C.
1221 (2016). Crystal Structure of a Full-Length Human Tetraspanin Reveals a Cholesterol-Binding Pocket.
1222 *Cell*, *167*(4). https://doi.org/10.1016/j.cell.2016.09.056
1223 Zimmerman, B., Kelly, B., McMillan, B., Seegar, T., Kruse, A., & Blacklow, S. (2016). Crystal Structure of
1224 Human Tetraspanin CD81 Reveals a Conserved Intramembrane Binding Cavity. *Cell*, *167*(4), 1041–1051.
1225 https://doi.org/10.1016/j.cell.2016.09.056
1226 Zwerger, M., Jaalouk, D. E., Lombardi, M. L., Isermann, P., Mauermann, M., Dialynas, G., … Lammerding, J.
1227 (2013). Myopathic lamin mutations impair nuclear stability in cells and tissue and disrupt nucleo-
1228 cytoskeletal coupling. *Human Molecular Genetics*, *22*(12), 2335–2349. https://doi.org/10.109
1229

bioRxiv preprint doi: https://doi.org/10.1101/2020.09.18.301481; this version posted September 18, 2020. The copyright holder for this preprint (which was not certified by peer review) is the author/funder, who has granted bioRxiv a license to display the preprint in perpetuity. It is made available under aCC-BY-NC-ND 4.0 International license.

Belyaeva et al. Figure 1

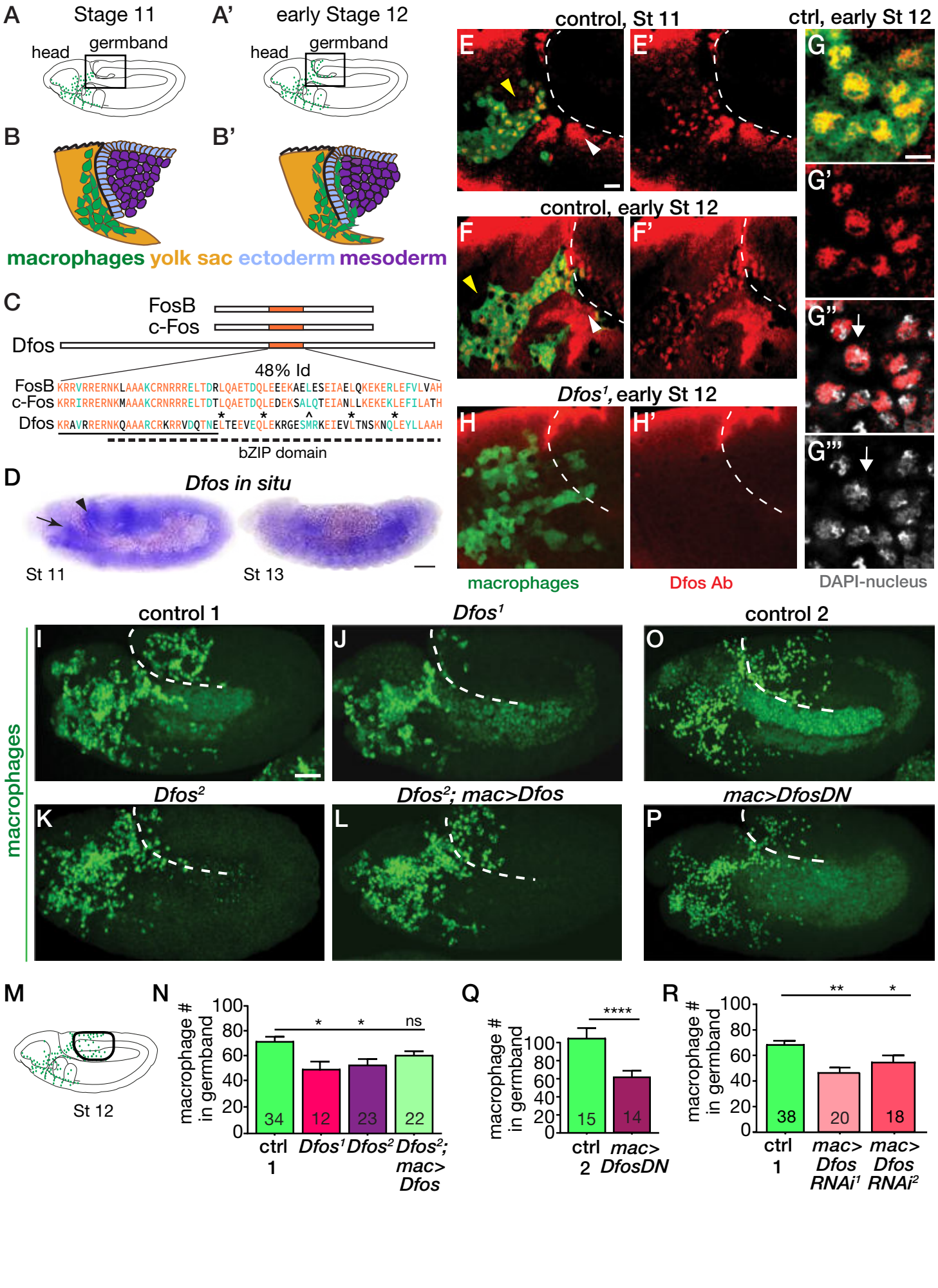

bioRxiv preprint doi: https://doi.org/10.1101/2020.09.18.301481; this version posted September 18, 2020. The copyright holder for this preprint (which was not certified by peer review) is the author/funder, who has granted bioRxiv a license to display the preprint in perpetuity. It is made available under aCC-BY-NC-ND 4.0 International license.

Belyaeva et al, Figure 2

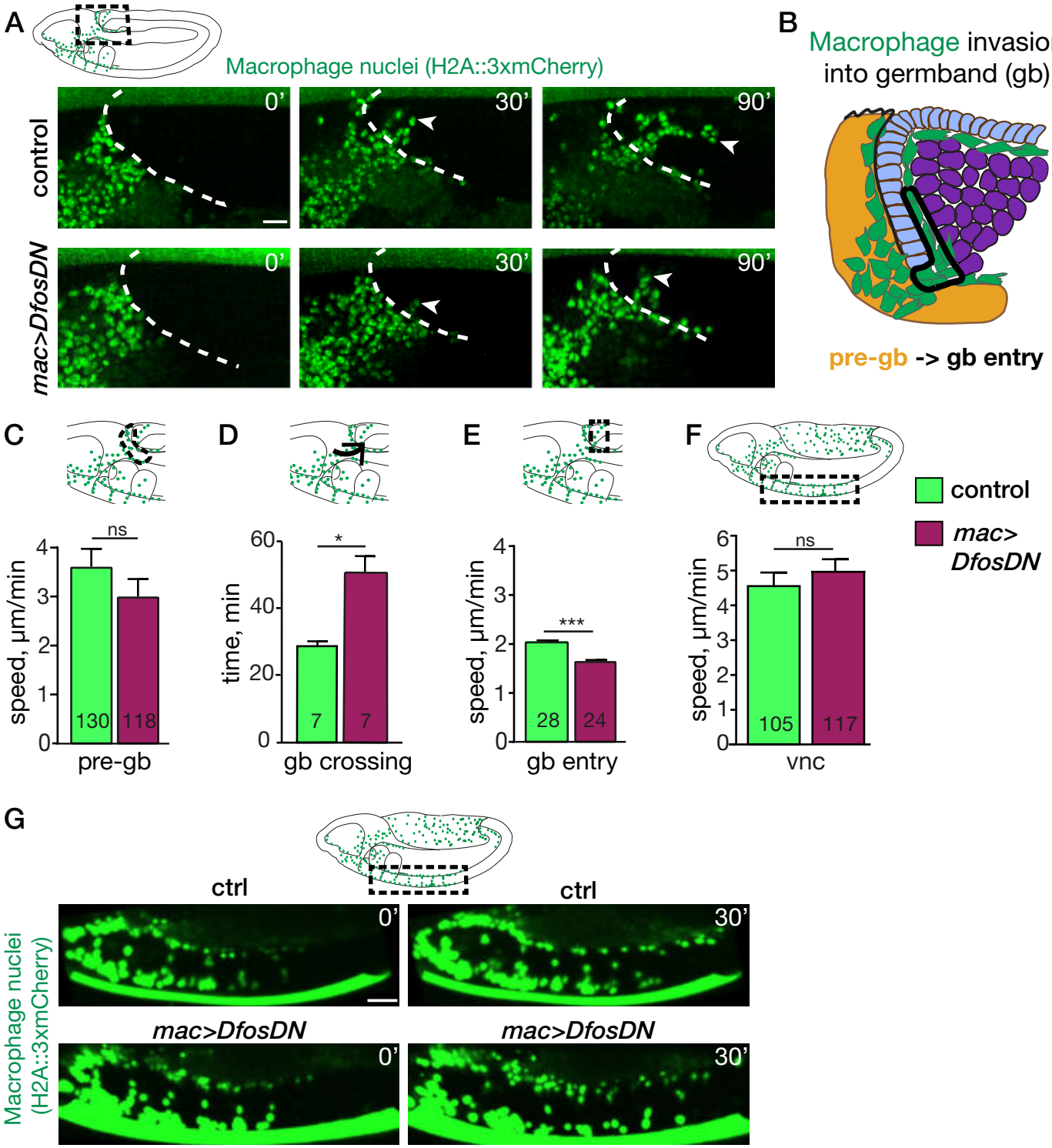

bioRxiv preprint doi: https://doi.org/10.1101/2020.09.18.301481; this version posted September 18, 2020. The copyright holder for this preprint (which was not certified by peer review) is the author/funder, who has granted bioRxiv a license to display the preprint in perpetuity. It is made available under aCC-BY-NC-ND 4.0 International license.

Belyaeva et al, Figure 3

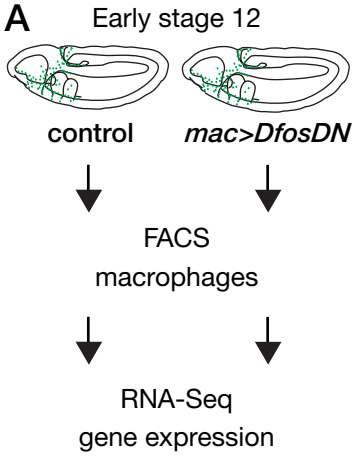

B

Gene	Possible Cellular Function	Mouse Ortholog Protein	Identity
cher	actin crosslinking	Filamin A	53%
CG42402	homophilic adhesion	Protein eva-1 homolog	35%
TM4SF	cell membrane organisation	Tetraspanin-6	24%
Xrp1	adhesion down-regulation	Epiglycan	22%
Dhc36C	cargo transport	Dynein axonemal, heavy chain 7C	57%
CG42260	ion transport	Cyclic nucleotide-gated olfact. channel	50%
Tspo	mitochondrial transport	Translocator protein	46%
GstT4	detoxification (glutathione transfer)	Glutathione S-transferase theta-3	39%
CG14204	acetyl-CoA metabolism	O-acetyltransferase like protein	27%
CG31337	proteolysis	no ortholog	NA

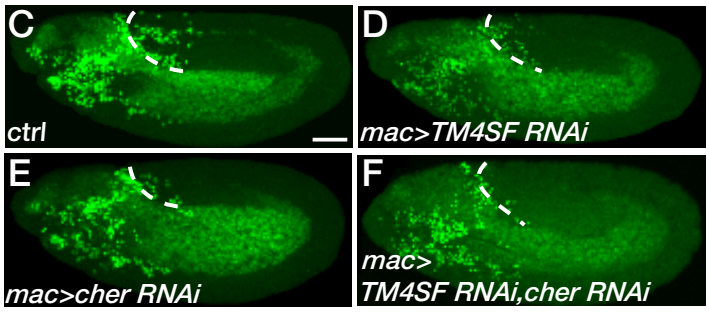

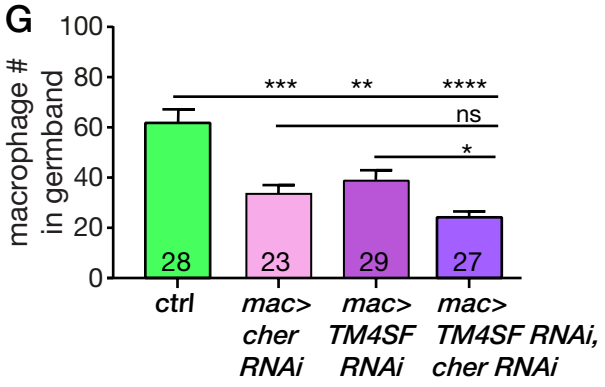

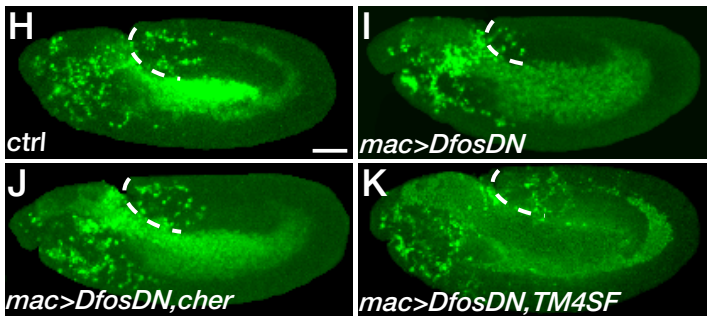

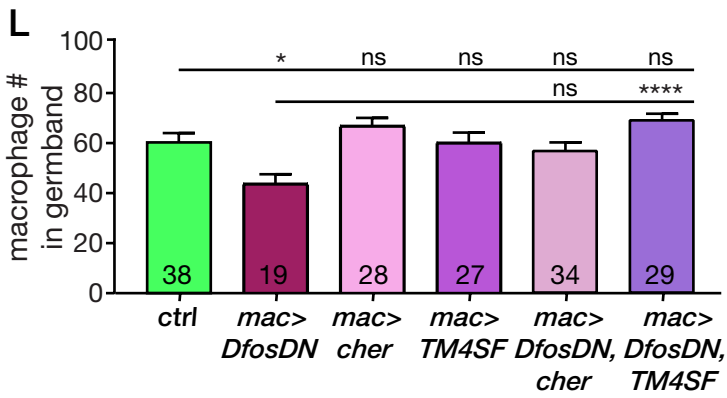

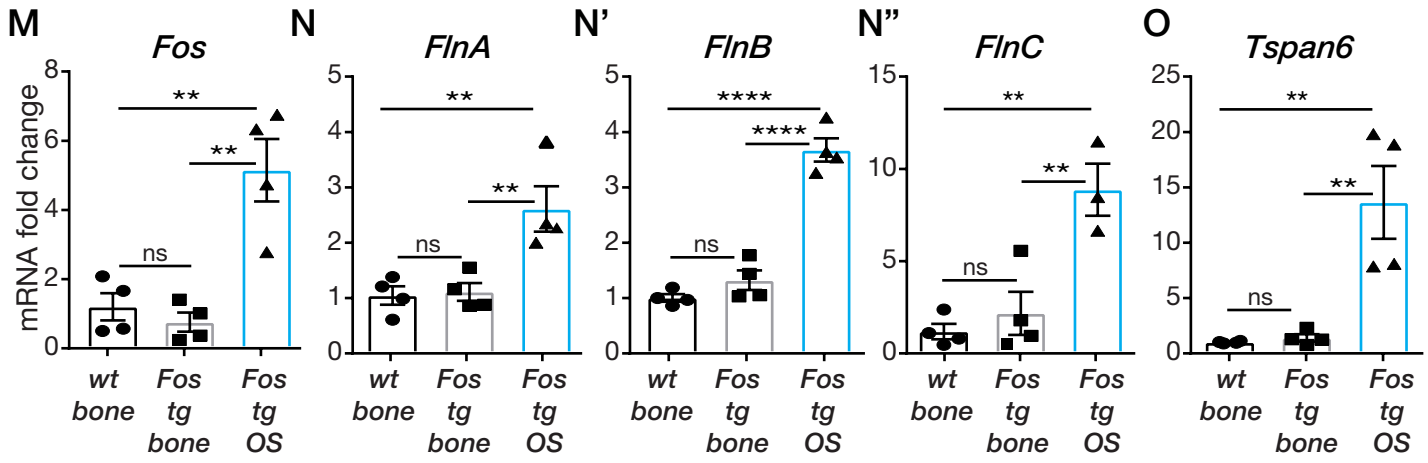

bioRxiv preprint doi: https://doi.org/10.1101/2020.09.18.301481; this version posted September 18, 2020. The copyright holder for this preprint (which was not certified by peer review) is the author/funder, who has granted bioRxiv a license to display the preprint in perpetuity. It is made available under aCC-BY-NC-ND 4.0 International license.

Belyaeva et al, Figure 4

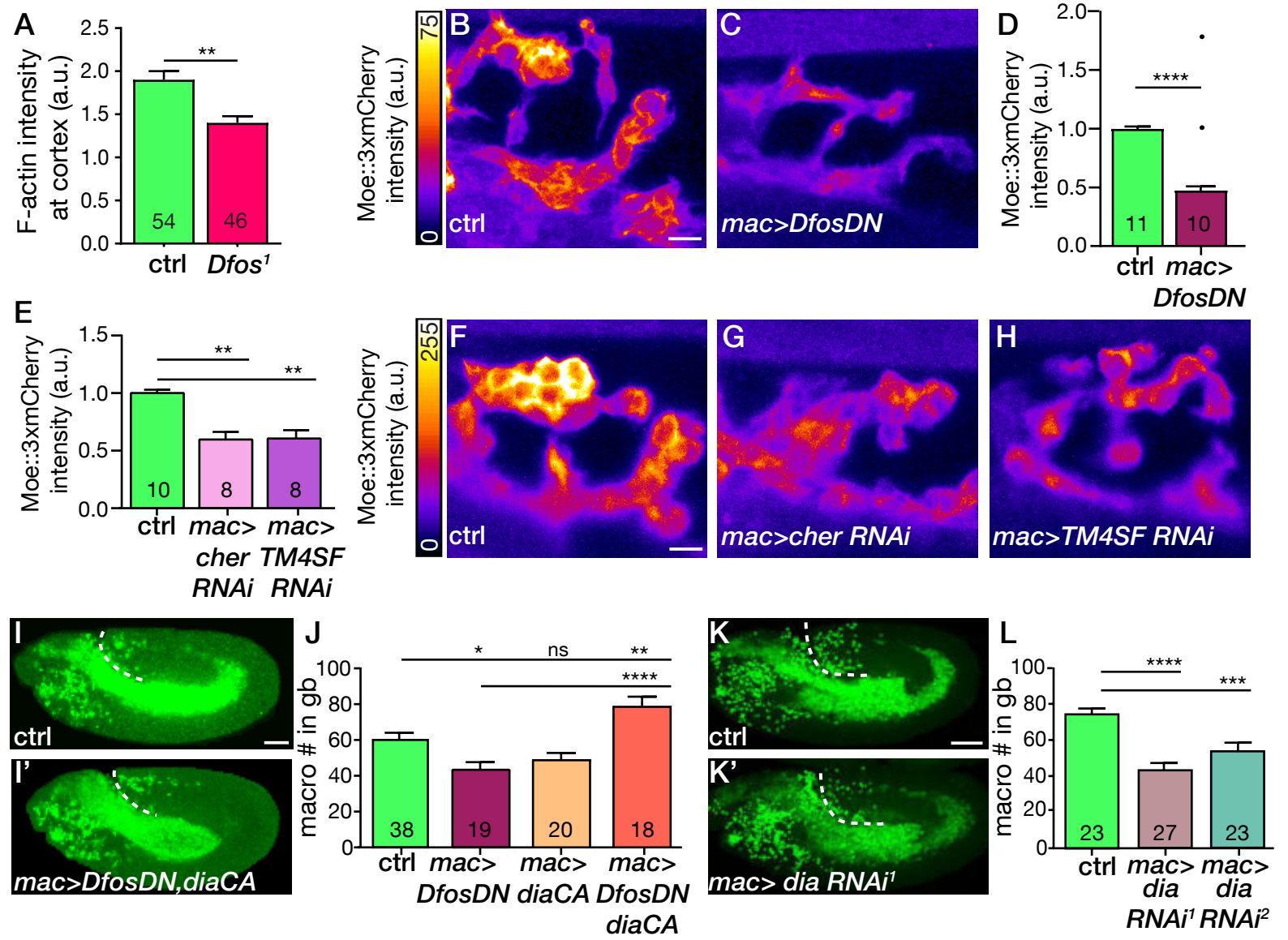

Belyaeva et al. Figure 5

bioRxiv preprint doi: https://doi.org/10.1101/2020.09.18.301481; this version posted September 18, 2020. The copyright holder for this preprint (which was not certified by peer review) is the author/funder, who has granted bioRxiv a license to display the preprint in perpetuity. It is made available under aCC-BY-NC-ND 4.0 International license.

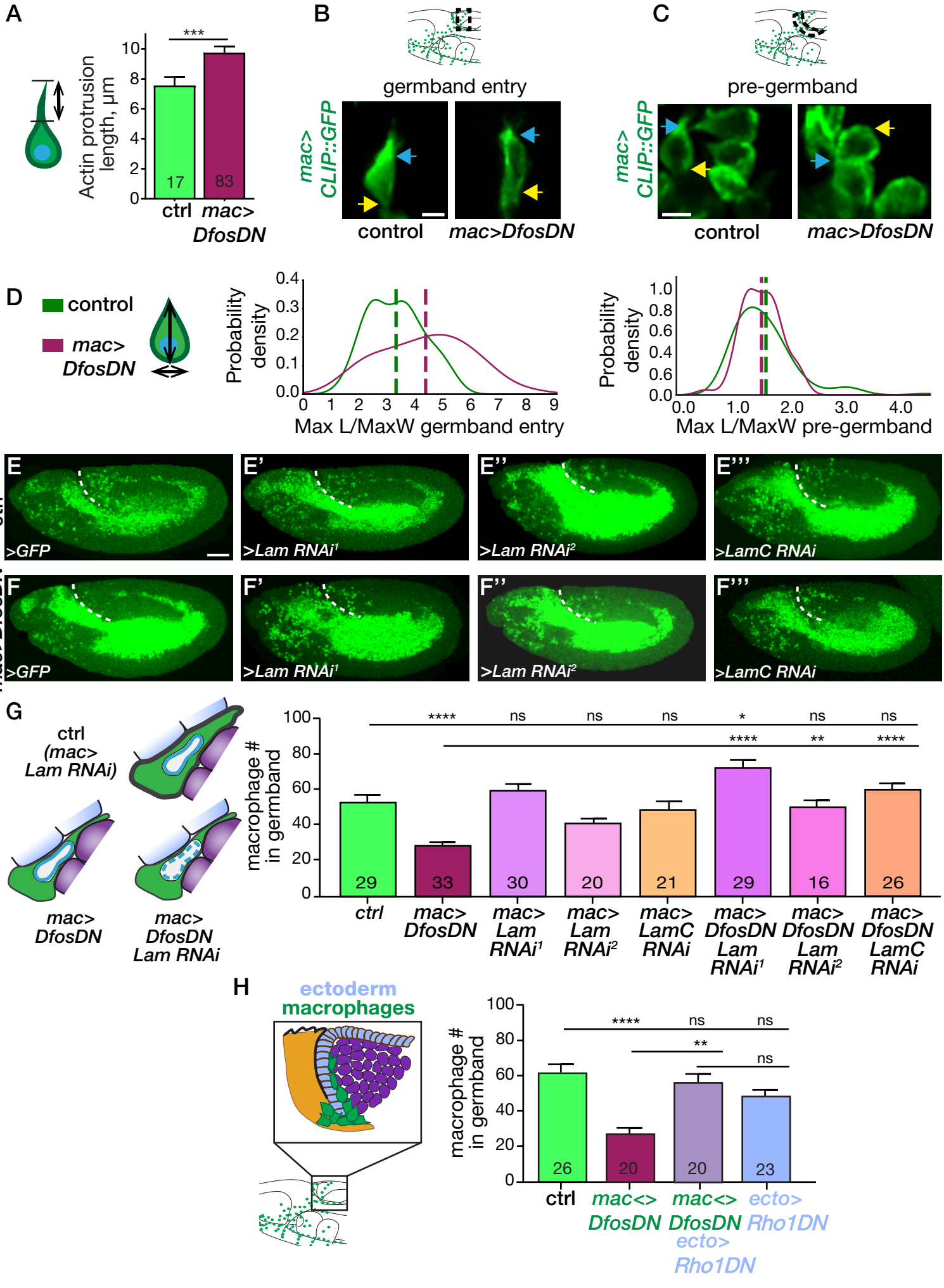

bioRxiv preprint doi: https://doi.org/10.1101/2020.09.18.301481; this version posted September 18, 2020. The copyright holder for this preprint (which was not certified by peer review) is the author/funder, who has granted bioRxiv a license to display the preprint in perpetuity. It is made available under aCC-BY-NC-ND 4.0 International license.

Belyaeva et al. Figure 6